Impact of micro-alloying in ion-irradiated nickel: From the inhibition of point-defect cluster diffusion by thermal segregation to the change of dislocation loop nature

Kan Ma, Brigitte Décamps, Liangzhao Huang, Robin E. Schäublin, Jörg F. Löffler, Anna Fraczkiewicz, Maylise Nastar, Frédéric Prima, Marie Loyer-Prost

To cite this version:

Kan Ma, Brigitte Décamps, Liangzhao Huang, Robin E. Schäublin, Jörg F. Löffler, et al.. Impact of micro-alloying in ion-irradiated nickel: From the inhibition of point-defect cluster diffusion by thermal segregation to the change of dislocation loop nature. Acta Materialia, 2023, 246, pp.118656. 10.1016/j.actamat.2022.118656 . hal-04011017

HAL Id: hal-04011017
https://hal.science/hal-04011017v1

Submitted on 4 Jul 2023

Impact of micro-alloying in ion-irradiated nickel: from the inhibition of point-defect cluster diffusion by thermal segregation to the change of dislocation loop nature

Kan Ma[a,e,1], Brigitte Décamps[b], Liangzhao Huang[a], Robin E. Schäublin[c], Jörg F. Löffler[c], Anna Fraczkiewicz[d], Maylise Nastar[a], Frédéric Prima[e] and Marie Loyer-Prost[a*].

[a] Université Paris-Saclay, CEA, Service de Recherches de Métallurgie Physique, 91191, Gif-sur-Yvette, France.

[b] Laboratoire de Physique des 2 infinis Irène Joliot-Curie (IJCLab), CNRS/IN2P3, Université Paris-Saclay, 91400 Orsay, France;

[c] Laboratory of Metal Physics and Technology, Department of Materials, ETH Zürich, Vladimir-Prelog-Weg 4, 8093, Zürich, Switzerland

[d] MINES Saint-Etienne, Université de Lyon, CNRS, UMR 5307 LGF, Centre SMS, 42023 Saint-Etienne, France ;

[e] PSL Research University, Chimie ParisTech-CNRS, Institut de Recherche de Chimie Paris, Paris, France.

[1] Now at the School of Metallurgy and Materials, University of Birmingham B15 2TT, United Kingdom.

Corresponding author: Marie LOYER-PROST.

Mail: marie.loyer-prost@cea.fr

Courrier: CEA Saclay, DES/ISAS/DMN/SRMP/JANNUS (Bât 126, pièce 58), PC. 162, 91191 Gif-sur-Yvette CEDEX, France.

Telephone +33 (0)1 69 08 24 68.

Abstract (250 words limited)

Micro-alloying strongly affects the incubation period of void swelling in irradiated face-centered cubic materials. However, the underlying mechanism, which relates to the formation of dislocation loops, is still unclear. Here, we investigate pure Ni, Ni-0.4wt.%Cr and Ni-0.4/0.8/1.2wt.%Ti as model materials, to gain insight into the solute effects on the loops evolution in the early stage of irradiation. The dislocation loop characteristics (mobility, Burgers vector, nature) are studied using *in situ* transmission electron microscopy and *ex situ* irradiation with Ni^+ ions at 450°C and 510°C for doses from 0.06 to 0.7 dpa. It appears that a tiny amount of Ti effectively increases the loop density, reduces the loop mobility and the stacking fault energy. It leads to an equal distribution among a/2<110> perfect loop families. It also stabilizes self-interstitial loops against vacancy loops depending on Ti content and temperature. Our modeling of radiation-induced segregation, based on experiments and recent *ab initio* calculations of flux couplings, predicts a Cr enrichment and a Ti depletion nearby dislocation loops. It is in good agreement with our observations by X-ray spectroscopy in TEM and by atom probe tomography. However, the lowered loop mobility must be the signature of a thermal segregation rather than the impact of radiation-induced depletion. Indeed, oversized Ti atoms subsequently trapped at strained lattice sites around the dislocation line of the loop due to thermal segregation would inhibit its diffusion. This opens new perspectives for future experimental investigations and radiation effect modeling.

5 keywords

irradiation, micro-alloying, dislocation loop nature, radiation-induced segregation, thermodynamics.

Graphical abstract

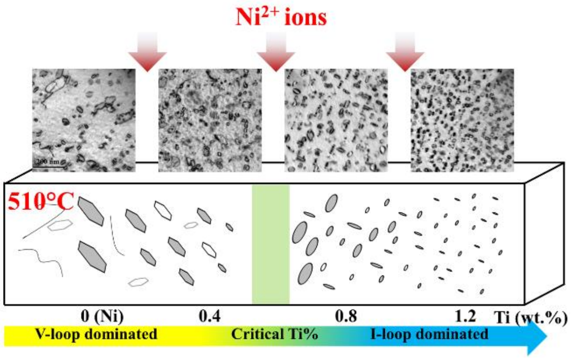

1. Introduction

Austenitic stainless steels are foreseen as cladding materials for future sodium-cooled fast fission reactors (SFRs) [1]. The main limitation of austenitic steels is the radiation-induced void swelling, which is a complex phenomenon [1–3]. It starts with an incubation period during which no macroscopic volume extension takes place but microstructure evolves. Once a threshold dose has been reached, swelling kicks in and quickly exhibits a steady rate. The latter is almost insensitive to the steel composition and its initial metallurgical state. Conversely, the onset of swelling is strongly affected by the chemistry and initial microstructure of the steel and the changes in the microstructure during the incubation [4–6]. Further, it seems to correlate to the onset of a steady state in irradiation-induced dislocations loops and lines. Besides, a change in the Ni to Cr content ratio or micro-alloying with minor solutes such as Ti can strongly delay the onset of void swelling of austenitic steels [7–11]. Notwithstanding, further improvements of their radiation tolerance can be envisaged, but require a better understanding on the fundamental mechanisms of the impact of solutes on radiation damage in the early stages of irradiation.

As austenitic steels have a complex composition with dozens of alloying elements, the identification of the role of one of these elements on the microstructure evolution or the mechanisms at play is harsh. One way to avoid this complexity is to employ model alloys as it is commonly done for body-centered cubic steels [12–15]. The face-centered cubic (fcc) crystal structure of austenitic steels is held by the addition of nickel. A simple model system for austenitic steels is therefore a material composed essentially of nickel (Ni), either as pure Ni or its alloys with other elements such as Cr [16,17]. The study of Ni-based model alloys is relevant not only for a better comprehension of the behavior of austenitic steels under irradiation but also for complex Ni-based alloys. Complex Ni-based alloys are indeed considered as promising candidates materials for Gen IV reactors such as molten salt reactors and also suffer from radiation-induced swelling [18].

Ni-based alloys and austenitic steels share the same type of defects after irradiation. Irradiation leads by knocking out atoms from their lattice site to the formation of point defects (PDs) in the form of vacancies and self-interstitial atoms (SIAs) that can condense in the fcc structure into voids, stacking fault tetrahedra and dislocation loops. Pure nickel (Ni) has been extensively studied [19–22] which provides some insight into the mechanism of radiation damage in fcc structure. In the early stage of irradiation, dislocation loops dominate the microstructure in Ni-based materials over the temperature range of fast reactors and the formation of dislocation network is responsible for the onset of void formation [16,19,23–27]. In pure nickel, Frank loops with a Burgers vector a/3<111> and perfect loops with a Burgers vector a/2<110> were both detected following neutron [19,21], electron [23,24,28] and ion [26,27,29–32] irradiations. The Frank loop nature (interstitial-type or vacancy-type) and their growth under irradiation attract particular attention as their formation energy is lower than the corresponding perfect loops [33,34]. They are two characteristic features strictly related to the diffusion of point defects (PDs) and point defect clustering tendencies which allows us to unravel the mechanism of radiation damage. In terms of the loop nature, in pure nickel, most studies suggested that radiation-induced Frank loops are interstitial-type. However, recent studies revealed that, up to 1 µm below irradiated surfaces, Frank loops can also be vacancy-type in self-ion irradiated Ni at high temperatures (over 450°C) [17,35].

So what are the fundamental mechanisms that drive the loops’ nature in pure Ni ? The interstitial nature of Frank loops after electron and light-ion irradiations in Ni is explained by conventional rate theory based on the dislocation bias model [36–39]. In general, dislocation loops induce a bias larger than any other sink (surface, voids) [38,40], meaning in this instance that they absorb more interstitials than vacancies. This leads to the growth of interstitial loops and the shrinkage of vacancy loops. Note that the conventional rate theory implies that (i) PDs are continuously and uniformly produced in the form of Frenkel pairs and (ii) all PDs are equally accessible to dislocations. These assumptions may not be satisfied in the case of heavy ion irradiation: the clustering of point defects within ion-induced cascades and the heterogeneous spatial distribution of vacancy or interstitial clusters may indeed lead to an unequal proportion of freely migrating vacancies and SIAs after ion irradiation, which leads to the so-called production bias model [41]. In Ni, interstitial clusters experience long-distance 1D motion along <110> directions and can subsequently escape from the damage production zones [42,43]. The production bias model combined with 1D motion of interstitial clusters (I-clusters) allowed us to explain the growth of vacancy loops in self-ion irradiated Ni [35]. In effect, it appears that, if the freely migrating interstitial population is reduced by this production bias and the ensuing loss of interstitials to surfaces exceeds a critical value, vacancy loop growth becomes favorable.

The nature of Frank loops thus seems to be sensitive not only to the conditions of irradiation but also to the presence of impurities: in Ni-based alloys irradiated at 450°C, a drastic effect of a low concentration of solute on the Frank loop nature has been shown [17]. In fact, in self-ion irradiated Ni-0.4Cr and Ni-0.4Ti (wt.%) alloys, Frank loops have been identified as interstitial-type [17]. Another key question raises: how solutes affect dislocation loop nature? In concentrated alloys, solute effects in alloys are related to specific fluctuations of the lattice distortion and short-range order which can modify the defect migration barrier landscape and trap the freely migrating defects [19,31,44–46]. In nickel, an increase of the solute content generally increases the average migration barriers of defects [46,47]. Some authors suggested that, in concentrated Ni alloys, the related increase of the migration barrier of I-clusters changes their 1D motion into a complex 3D motion made of short-distance 1D jumps [43,47]. I-clusters can subsequently remain longer in the damage zone and in turn favor the growth of interstitial loops. Also, the addition of solutes was shown to stabilize dislocation loops *i.e.* increasing their density whilst reducing mobility in concentrated Ni-Cu alloys (Cu and Ni forms complete solid solution) but loop nature was not addressed in these studies [48,49]. However, are those mechanisms transferable to dilute alloys? In concentrated alloys, simple diffusion models are sufficient to explain diffusion and flux couplings of the major elements [50] but in dilute alloys detailed modelling of local composition effects on point defect frequencies might be required. The thermodynamic role of dilute species in Ni-based systems under irradiation is rarely discussed because it is often difficult to identify it in the realm of non-equilibrium solute redistribution phenomena controlled by irradiation. In particular, radiation-induced segregation (RIS) resulting from the flux couplings between PDs and solute atoms may be opposite to the one induced thermally. In addition, the typical width of a RIS profile e.g. across grain boundary is a few tens of nanometers, while thermal segregation extends over at most one or two atomic planes [51]. Besides, thermal segregation may be hidden by RIS. While detailed studies of the effect of a change in the solute content in dilute systems on irradiation-induced microstructures would improve our understanding of the role of solutes, they are scarce. Therefore, a detailed characterization of micro-alloying on dislocation loops is thus highly desired. This would provide a better understanding of the impact of the solute atoms on the radiation-induced phenomena and precious experimental data for multi-scale modeling to eventually predict and mitigate radiation-induced swelling in austenitic steels and complex Ni-based alloys.

~~In a recent paper focused on the swelling behavior of neutron-irradiated Ni-based dilute alloys, it was proposed that the addition of solutes such as Ti, Si and Al has an impact on the loop formation and unfaulting process, which may be the reason altering the swelling behavior [16]. This study was however focused on the solute effects on the void formation at high irradiation doses, which don't allow identifying the onset of swelling. Besides, the influence of solute addition on the dislocation loops Burgers vector and nature was not reported. Note that to our knowledge this was never reported for the early stage of irradiation in dilute systems. A detailed characterization of solute effects on dislocation loops at that stage is thus highly desired~~.

The aim of this work is to investigate the influence of dilute species, namely Ti and Cr, on the evolution of the dislocation loop microstructure in nickel under irradiation at doses lower than the one for the onset of swelling at 510 °C, which is relevant to future SFRs. To that end, we performed transmission electron microscopy (TEM) in-situ irradiation experiments to closely follow the evolution of the dislocation microstructure, and post-characterized the microstructure after the irradiation. In situ TEM irradiation is a very powerful tool to get an insight in the microstructural evolution of materials [29,52–55]. As irradiated samples are very thin (below 300 nm thick), the proximity of free surfaces, a sink for PDs created under irradiation, can greatly influence the evolution observed and compromise any study of solute effects on microstructural evolution. An essential guideline to avoid these surface effects for pure nickel was previously established and opened new fields of studies for Ni-alloys such as this work [35]. The guideline was therefore applied in this study. We performed a campaign of in-situ high energy self-ion irradiations with 2 MeV Ni^{2+} ions in thin foils, with controlled thicknesses, of high purity Ni-0.4/0.8/1.2Ti (wt.%) alloys. To assess the impact on temperature, we performed complementary ex-situ irradiation at 450°C with Ni^{2+} 5MeV on thin foils samples. The influence of the Ti content and temperature on the microstructure was analyzed. The impact of Cr was investigated with a high purity Ni-0.4Cr (in wt.%) alloy with the same irradiation conditions. From the observed microstructural evolution, we extracted the mobility of dislocation loops as well as their size and number density. We subsequently deduced their growth rate. We performed post-irradiation characterizations to obtain the nature, Burgers vector, size and density of the dislocation loops. In addition, we performed ex-situ irradiations at 450°C in order to comparatively study the impact of the temperature on Frank loop nature.

With these experiments, we assessed, firstly, the influence of micro-alloying (addition of Ti or Cr) on the microstructural evolution, radiation-induced loops type (Burgers vector) and nature (interstitial or vacancy) and, secondly, the impact of the solute content coupled with the irradiation temperature on these loop characteristics. Finally, we applied diffusion theory and mean field rate theory to model the experimental results. It allowed us to reveal fundamentally new aspects of the impact of solute on the radiation-induced dislocation loops in austenitic steel model alloys. It challenges our understanding of irradiation effects and the balance between thermal and irradiation-induced segregation.

2. Methods

2.1 Studied materials

Rods of pure nickel (Ni), Ni-0.4 wt.% Ti (Ni-0.4Ti in short) and Ni-0.4 wt.% Cr (Ni-0.4Cr) were manufactured by cold crucible induction melting at MINES Saint

Etienne (EMSE) with an impurity content (in ppm) in O, C, N and S of respectively 3, 8, 2 and 2 for Ni, 14, 2, 1 and 4 for Ni-0.4Ti and 6, 4, 8 and 1 for Ni-0.4Cr. Two other nickel-titanium alloys Ni-0.8 wt.% Ti (Ni-0.8Ti) and Ni-1.2 wt.% Ti (Ni-1.2Ti) were also prepared by induction melting in the Service de Recherches de Métallurgie Physique (SRMP) using pure nickel (>99.99 wt.%) and pure titanium (>99.99 wt.%) from Goodfellow company.

The annealing conditions and TEM sample preparation were presented in [35]. The initial dislocation density is low (about 10^{10} m^{-2}) before irradiation, which means that there is at least about 10μm between dislocations in the thin foil where regions of interest for the TEM observations are less than 300 nm thick. This indicates that the initial dislocations won't significantly affect the evolution of the nanometer-scaled radiation-induced defects of interest in this study.

2.2 Irradiation conditions

In-situ irradiations were performed at the JANNUS-Orsay platform at Laboratoire de Physique des 2 Infinis Irène Joliot-Curie (IJCLab). Thin foils were in-situ irradiated in a 200 kV FEI Tecnai G2 TEM by a 2 MeV Ni^{2+} rastered beam produced by a 2 MV tandem Van de Graaff accelerator (named ARAMIS). The vacuum level of the specimen chamber was 10^{-5} Pa. The irradiation temperature was 510 °C monitored by a Gatan double-tilt heating holder with an estimated uncertainty of 25 °C. The ion flux was of $4 \pm 0.8 \times 10^{11}$ ions cm^{-2} s^{-1}. Final fluences were $9 \pm 1.8 \times 10^{13}$ ions cm^{-2} and $2.7 \pm 0.4 \times 10^{14}$ ions cm^{-2}. Irradiations were imaged in TEM under a two-beam condition with a diffraction vectors **g**={200} or {111} in kinematical bright-field (KBF) mode ($s_g>0$). During irradiation, the microstructure evolution was recorded at 30 frames per second using a GATAN MultiScan 2k x 2k charge-coupled device high-resolution camera and analyzed after irradiation. It is worth noting that, in Ni, Ni-0.4Cr and Ni-0.4Ti specimens, in-situ observations and post-irradiation characterization are performed in zones thicker than 200 nm to minimize the effect of free surfaces [35]. In order to better characterize individual loops when in high number densities, in Ni-0.8Ti and Ni-1.2Ti, the observation was performed in thinner areas, typically 120 nm, to minimize the overlap of loops in the image.

The penetration depth of the ions and the corresponding damage profiles were calculated by the Stopping Range of Ions in Matter (SRIM) 2013 code [56] using the Kinchin-Pease option with a displacement threshold energy of 40 eV [3,57]. To double check the calculation, they were also calculated by the recently developed Monte Carlo code Iradina [58] with the same input parameters as SRIM. The corresponding profiles calculated by both codes are shown in Fig. A. 1. They are in good agreement, both on the displacement damage and the implantation profile, with the Bragg peak located at around 500 nm from the free surface. The damage profile is rather broad (Fig. A. 1): the thickness of the zones of interest for TEM being at most 300 nm, it indicates that the chosen ions energy allows a relatively homogeneous damage throughout the sample thickness. For practical purposes, the irradiation dose in samples was considered to be constant throughout the thickness. It was evaluated at a depth of 200 nm, yielding a value of 0.06 dpa for the lowest fluence and 0.18 dpa for the highest fluence. The analysis of the radiation-induced dislocation loops to obtain their Burgers vector and nature was performed using the g·b analysis method and stereoscopy, as detailed below. Most analyses were conducted after irradiation to 0.06 dpa, while the highest dose of 0.18 dpa was considered for those alloys exhibiting loops that at 0.06 dpa were too small for their analysis by TEM. The number of injected interstitials is relatively low (0.02 ppm per dpa) and its influence on microstructure is neglected.

Ex-situ irradiation experiments were conducted at the JANNuS-Saclay plaform using a rastered beam of 5 MeV Ni^{2+} ions on samples in the form of electropolished TEM disks. The irradiation temperature was 450 ± 10 °C monitored by 4 thermocouples in contact with the samples. The ion flux was of $2.1 \pm 0.5 \times 10^{11}$ ions cm^{-2} s^{-1}. Final fluence was $2.3 \pm 0.5 \times 10^{15}$ ions cm^{-2} with the dose at the implanted surface up to 0.7 dpa. Corresponding damage profiles are given in Fig. A. 1 in Appendix A.

2.3 Defect analysis

Besides the analysis of the video live records of the evolution of the microstructure during the irradiation, a thorough characterization of the irradiation-induced dislocation loops was performed ex-situ using a 200 kV FEI TECNAI G2 TEM with a LaB_6 filament located at SRMP laboratory in CEA-Saclay. TEM characterization methods are similar to the ones applied in [35]: (i) the longest distance within a given loop image was taken as its diameter. The error bar on the loop size is the standard deviation. (ii) The thickness of studied zones was measured using convergent electron beam diffraction (CBED) technique [59] with a {220} reflection and is used to calculated the number density of loops (in short, the loops density). The thickness measurement was double checked using electron energy loss spectroscopy (EELS) [59] in thin zones (40-120 nm) and stereo-microscopy technique [60] for all thicknesses. The error bar on the loop density is mainly due to the uncertainty on the thickness measurement, which amounts to about 10 %. (iii) The Burgers vectors analysis of individual loops was performed using the invisibility criterion or g·b analysis technique [39] and their nature was determined using the inside-outside method [61–63] with the finish to start right-handed (FSRH) convention. (iv) A statistical treatment [44] was applied to determine the fraction of Frank loops and perfect loops.

Energy dispersive X-ray spectroscopy (EDS) was used to measure the local variation of composition in our samples. The analyses were performed at ScopeM laboratory of ETH Zürich using a 200 kV FEI Talos F200X TEM equipped with the high-throughput Super-X EDS detector of Bruker.

3. Results

In this section, we first present the results of the TEM in situ irradiations at 510 °C of Ni-0.4Cr, Ni-0.4Ti, Ni-0.8Ti and Ni-1.2Ti alloys. This allows the study of the effect of micro-alloying on the evolution of the irradiation-induced dislocation loops in terms of their density and average size, growth rate and mobility. To ground the study of the solute effect, results are compared with data obtained with pure Ni that was reported in a previous paper [35]. The distribution of the loops nature and Burgers vector as determined by post irradiation analysis is also presented. The nature of the loops is then compared to the one observed in the samples irradiated ex situ at 450 °C to investigate the solute effect at different temperature.

3.1 Influence of micro-alloying on in-situ behavior (loops density, size, growth rate and mobility) at 510°C

Fig. 1 presents a selection of frames extracted from the videos acquired during the TEM in-situ irradiations. They exhibit the microstructural evolution of each sample irradiated at 510°C up to 0.06 dpa, corresponding with the applied dose rate to around 240 seconds of irradiation. Note that for Ni-0.4Ti, as the diffraction condition was poorly defined at the beginning of the in-situ irradiation, which resulted in low quality imaging, the microstructural evolution is shown only after 84 s (corresponding to a dose of 0.02 dpa). It appears that irradiation induces dislocation loops in all samples. Dislocation loops were quantified (Fig. 2): Fig. 2(a) and Fig. 2(b) show respectively their density and average size as a function of irradiation time. Both appear to increase monotonously with increasing dose in nearly all materials.

In pure Ni, the loop density and size reach saturation at respectively 50 s and 80 s, corresponding to a dose of respectively 0.013 and 0.02 dpa. The apparent decrease of the loops size with increasing dose after saturation is related to the merging of loops into dislocation lines, leading to the formation of a dislocation network.

In Ni-0.4Cr, the loops density and average size increase with the irradiation time and reach a maximum value at respectively 120 s and 180 s, corresponding to a dose of respectively 0.03 and 0.045 dpa. At the end of the irradiation, large loops are formed and start to merge. Compared to pure Ni, the presence of Cr in Ni decreases the loops density. However, while the average loops size is lower than the one in pure Ni in the early stages of irradiation, it increases to a higher value by the end of the irradiation, at a dose of 0.06 dpa. The lower density in Ni-0.4Cr allows loops to grow up to a larger size before merging. If the irradiation were pursued to a higher dose, the growing loops would start to merge, which in the end would result in a decrease of the average size like in pure Ni.

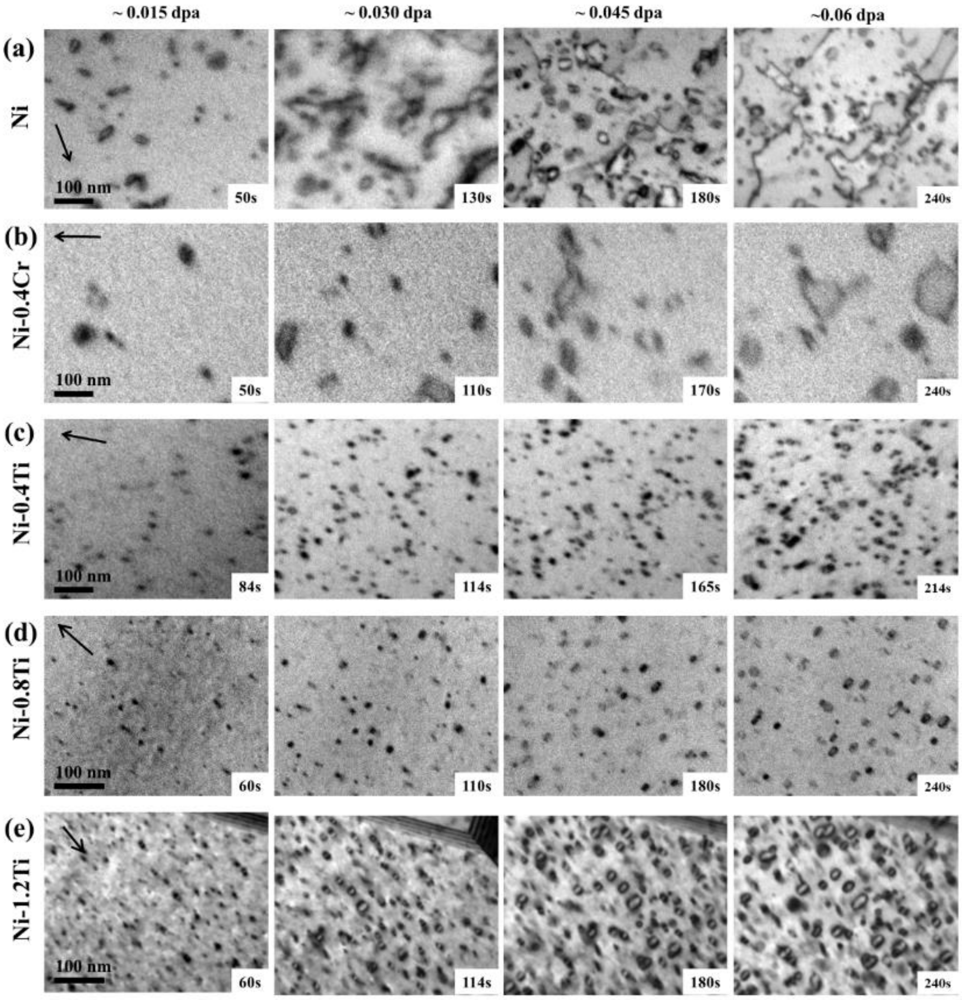

Fig. 1 TEM micrographs presenting the microstructural evolution of (a) Ni, (b) Ni-0.4Cr, (c) Ni-0.4Ti, (d) Ni-0.8Ti and (e) Ni-1.2Ti during TEM in-situ irradiation at 510°C as a function of the irradiation time (corresponding approximate dose indicated in the top). TEM micrographs recorded under two-beam bright field condition using **g** = {200} in (a,b,e) and **g** = {111} in (c,d). Diffraction vector and scale bar for each alloy are indicated in the first micrograph. Sample thickness is in (a) around 260 nm, (b,c) around 200 nm and in (c,d) around 120 nm.

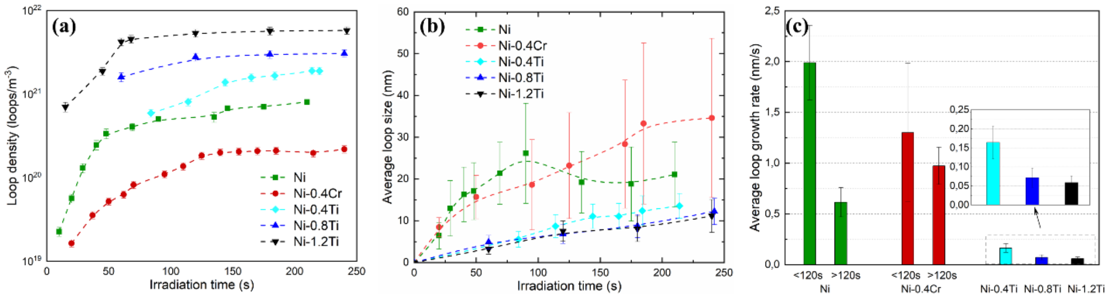

Fig. 2 Evolution of the irradiation-induced dislocation loops (a) density and (b) average size as a function of irradiation time, and (c) average growth rate of loops in each alloy. Note that 240 s of irradiation corresponds to a dose of 0.06 dpa.

In Ni-0.4Ti, the loop density increases, then reaches a maximum after around 200 s or 0.05 dpa, while in Ni-0.8Ti and Ni-1.2Ti, it increases more sharply and quickly reaches a maximum at about 60 s or 0.015 dpa. However, the loop size continuously increases until the end of irradiation. The final loops are small, and there is no merging of loops. These observations reveal that the addition of Ti strongly increases the density of loops but reduces their size. These effects are all the greater with higher Ti content.

The average loop growth rate is presented in Fig. 2(c). In Ni and Ni-0.4Cr, the loops growth rate was determined respectively before and after the maximum in the loops density. This maximum defines the beginning of the steady state regime of the dislocation loops evolution. It is worth noting that in both materials loops grow fast at the beginning of the irradiation as long as the number density of loops is small. When the loops number density reaches saturation, the loops growth rate gets slower. A natural explanation is that the increase of loops density represents an increase of the number of sinks for PDs, leading to a decrease of the PD concentrations and the loop growth rate. In all Ni-Ti alloys, as the loops growth rate variation with the radiation dose was insignificant, only its average value was assessed. It appears that it decreases as the Ti content increases.

During the in-situ irradiation, some dislocation loops move and disappear, probably at the free surfaces. Fig. 3a and b present the typical movement of loops in respectively Ni-0.4Cr and Ni-0.4Ti. The mobility of loops appears to be lower in Ni-0.4Cr and Ni-0.4Ti than in Ni, and in Ni-0.8Ti and Ni-1.2Ti loops are almost immobile. To evaluate the solute effect on loop mobility, two parameters were considered: the loop migration distance and velocity. Let us mention that the distances measured in the TEM images are inherently done on a 2D projection of the real 3D-displacements. It is thus difficult to determine the 3D migration path of a loop during the in-situ observation. To overcome this inconvenience, more than 10 loops slipping along different directions were analyzed, in order to obtain an average migration distance (presented in Fig. 3). Compared to Ni, the loop migration distance is slightly reduced in Ni-0.4Cr and strongly reduced in Ni-Ti alloys, suggesting that the loop mobility is highly suppressed by Ti and only slightly by Cr.

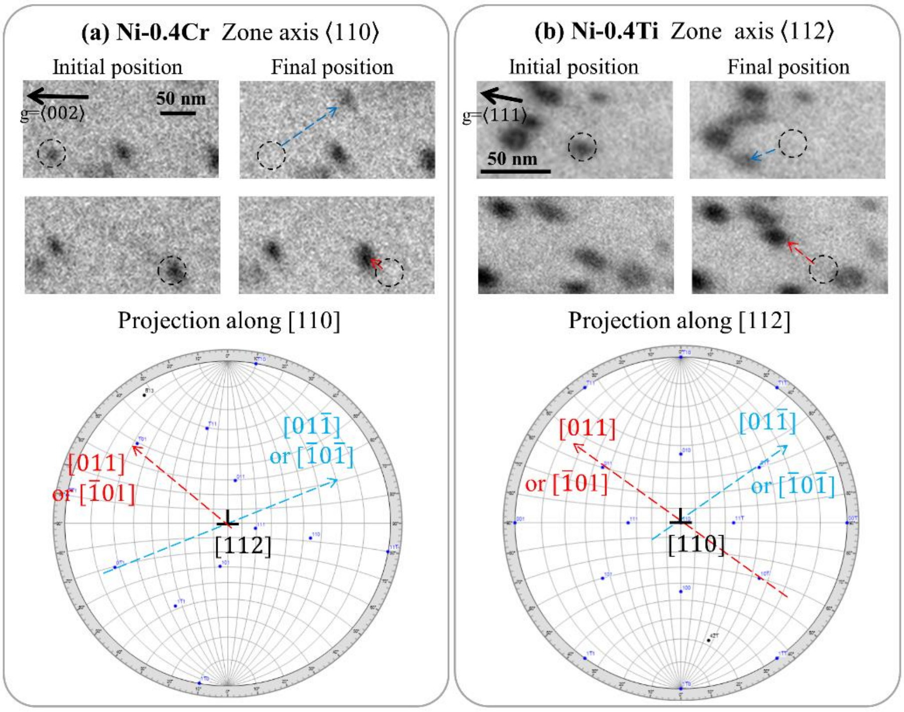

Fig. 3 Displacement of the dislocation loops during the in-situ irradiation at 510 °C in (a) Ni-0.4Cr and (b) Ni-0.4Ti: the displacement directions are indicated by blue and red arrows; Stereographic projections along the corresponding zone axis show that the displacement directions are <110>; the thickness in both cases is about 220 nm.

Table 1 Average migration distance of dislocation loops in pure Ni and Ni alloys irradiated in situ at 510°C to 0.06 dpa. The uncertainty corresponds to standard deviation.

Materials	Ni	Ni-0.4Cr	Ni-0.4Ti	Ni-0.8Ti	Ni-1.2Ti
Distance (nm)	108±39	80±22	18±5	≈ 0	≈ 0

3.2 Influence of micro-alloying on the Frank loop nature at 510°C

In all investigated alloys we observed different morphologies for the Frank dislocation loops, as shown in Fig. 4 and Fig. 5. A recent paper reported that vacancy Frank loops are segmented while interstitials ones are not [17]. Taking this into account, our analysis of the loops morphology indicates that the Frank loop nature changes from one material to another. In order to confirm this first observation, we relied on the inside-outside method to determine the nature of the dislocation loops [63]. The method was applied to more than ten loops in each material. We conclude that the nature of the Frank dislocation loops was strictly either interstitial or vacancy, depending on the material. TEM micrographs exhibiting typical Frank dislocation loops in Ni-0.4Cr and Ni-0.4Ti are presented in Fig. 4, while for Ni-0.8Ti and Ni-1.2Ti they are presented in Fig. 5. In Ni-0.4Cr, loops A, B and C are all Frank loops as they exhibit fringes contrast typical of a stacking fault inside the loop (Fig. 4 (a-b)). Based on the invisibility criterion [64], the Burgers vector of Frank loop A is $\mathbf{b}_A=\pm1/3[1\bar{1}1]$ as it is invisible for $\mathbf{g}=\bar{2}02$ (Fig. 4 (c)) and visible for $\mathbf{g}=0\bar{2}2$ (Fig. 4 (d)). The same analysis method leads to $\mathbf{b}_B=\mathbf{b}_C=\pm1/3[111]$ for loops B and C as they are invisible for these **g** (Fig. 4 (c-d)). Then, the **g** =±020 pair in Fig. 4 (i) shows the inside-outside behavior of loop A, B and C: A shows outside contrast for g=020 while B and C show inside contrast. Taking into account the FSRH convention [62], which relies on the clockwise convention of sign to determine the direction of a dislocation line, the outside contrast of loop A for **g**=020 leads to $\mathbf{g}.\mathbf{b}_A > 0$ and the inside contrast of loop B and C for the same **g** leads to $\mathbf{g}.\mathbf{b}_{B/C} < 0$. Finally we conclude that $\mathbf{b}_A=1/3[\bar{1}1\bar{1}]$ and $\mathbf{b}_{B/C}=1/3[\bar{1}\bar{1}\bar{1}]$ and that thus these loops are vacancy loops. The same method was applied to the Ni-0.4Ti alloys, as shown in Fig. 4 (e-h). It appears that in this alloy Frank loops are also vacancy in nature. These conclusions are supported by the observed polygonal morphology of the Frank loops in Ni-0.4Cr and Ni-0.4Ti, which is a signature of their vacancy nature [26].

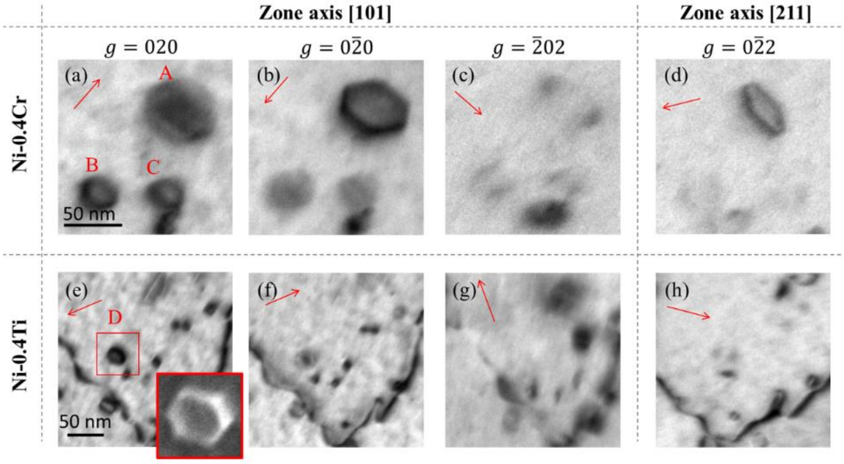

(i)

Loop	Contrast of loops			$\mathbf{g} \cdot \mathbf{b}$ for $\mathbf{g}$	$\mathbf{b}$	Nature
	$\pm\mathbf{b}$	$\mathbf{g} = [020]$	$-\mathbf{g} = [0\bar{2}0]$			
A	$\pm 1/3[1\bar{1}1]$	outside	inside	>0	$1/3\ [\bar{1}1\bar{1}]$	vacancy
B, C D	$\pm 1/3[111]$	inside	outside	<0	$1/3\ [\bar{1}\bar{1}\bar{1}]$	vacancy

Fig. 4 Determination of the nature of Frank loops in Ni-0.4Ti and Ni-0.4Cr irradiated at 510°C. TEM micrographs showing the loops contrast as a function of **g** (marked above and in the images) in (a-d) Ni-0.4Cr and (e-h) Ni-0.4Ti. Dark Field Weak Beam (DFWB) image in (e) showing the morphology of loop D in (i) Table for the determination of Frank loops nature.

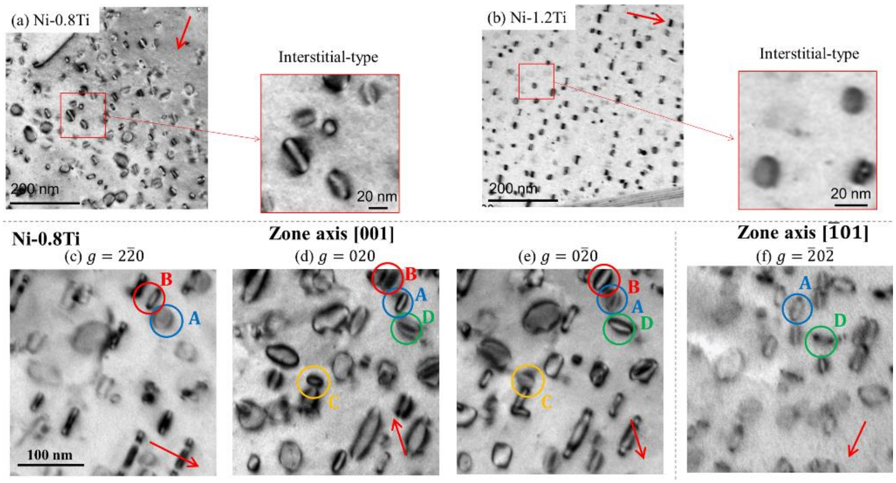

(g)

Loop	Contrast of loops along [001]			g. b for g	b	Nature
	b direction	$\mathbf{g} = [020]$	$-\mathbf{g} = [0\bar{2}0]$			
A	$[1\bar{1}1]$	inside	outside	<0	$a_0/3[1\bar{1}1]$	interstitial
B	$[\bar{1}11]$	outside	inside	>0	$a_0/3[\bar{1}11]$	interstitial
C	$[11\bar{1}]$	inside	outside	<0	$a_0/3[\bar{1}\bar{1}1]$	interstitial
D	$[111]$	outside	inside	>0	$a_0/3[1\bar{1}1]$	interstitial

Fig. 5 Determination of the nature of Frank loops in Ni-0.8Ti and Ni-1.2Ti irradiated at 510 °C to a dose of 0.18 dpa. TEM micrographs showing the Frank loop morphology in (a) Ni-0.8Ti and (b) Ni-1.2Ti. (c-f) Visibility of Frank loops as a function of **g** (marked above and in the images) and (g) table for the determination of Frank loops nature in Ni-0.8Ti. Sample thickness is around 120 nm. All identified loops are interstitial.

Conversely, Frank loops in Ni-0.8Ti and Ni-1.2Ti appear to be interstitial in nature, whatever their Burgers vectors. An example of the loop analysis in Ni-0.8Ti is shown in Fig. 5 (c-f). The Burgers vector analysis of the loops A, B, C and D lead to $\mathbf{b}_A=\pm1/3[1\bar{1}1]$, $\mathbf{b}_B=\pm1/3[1\bar{1}\bar{1}]$, $\mathbf{b}_C=\pm1/3[11\bar{1}]$ and $\mathbf{b}_D=\pm1/3[111]$. Their inside-outside contrast behavior shows that $\mathbf{b}_A=1/3[1\bar{1}1]$, $\mathbf{b}_B=1/3[\bar{1}11]$, $\mathbf{b}_C=1/3[\overline{11}1]$ and $\mathbf{b}_D=1/3[111]$.

The change of the Frank loop nature from 0.4wt.%Ti to 0.8wt.%Ti at 510°C indicates that there is a critical Ti concentration $C_{Ti}^{c}(T)$, which may depend on temperature, around which it occurs. For a given temperature, when the Ti concentration, C_{Ti}, is lower than the critical value ($C_{Ti}<C_{Ti}^{c}$), the microstructure is dominated by vacancy-type defects, whereas, when $C_{Ti}>C_{Ti}^{c}$, the microstructure is dominated by interstitial-type defects. As shown previously [35], the effect of surfaces on the microstructure strongly depends on the dominating point defect population. We expect then an effect of Ti on the change of the microstructure with the sample thickness.

3.3 Influence of micro-alloying on the loops Burgers vector

Note that the loops that are mobile in the fcc structure are perfect loops with a Burgers vector 1/2 <110>. In our study, the projected glide direction of the mobile dislocation loops in Ni, Ni-0.4Cr and Ni-0.4Ti was always parallel to <110> directions (Fig. 3). This indicates that the observed loops gliding in pure Ni and the Ni alloys were perfect loops. Besides, we observed that the glide of perfect loops in Ni induces a heterogenous distribution of their Burgers vectors. As the loops mobility is clearly affected by the addition of solutes, it is worth investigating their effect on the partition of loops between the Frank ones and the perfect ones using the statistical method presented in [65], which is based on the analysis of the loops Burgers vector using the g·b analysis method.

The statistical method requires to count the number of visible dislocation loops under at least four diffraction conditions defined by their diffraction vector **g**, with at least one non-coplanar vector [65]. To optimize the statistics, within the mechanical limit of sample tilting, 5 **g**, 7 **g**, 5 **g** and 6 **g** along at least two zone axes were used respectively in Ni-0.4Cr, Ni-0.4Ti, Ni-0.8Ti and Ni-1.2Ti. The used vector, **g,** and the corresponding observed loops density is listed in Appendix B. From the density of loops deduced from the visible ones for each **g**, one can infer the absolute density of loops per loops' Burgers vector (1/3<111> or 1/2<110>) or family type (Frank or perfect, respectively). To evaluate the proportion of each family of loops, we divide the density of a given family by the sum of the density of each family.

Fig. 6 (a-e) presents the distribution of the Burgers vectors for each material. The distribution of a given loops Burgers vector type among its different possible specific Burgers vectors is always equiprobable for the Frank loops, while the distribution for the perfect loops depends on the material. In effect, the distribution is strongly heterogeneous in pure Ni, slightly heterogeneous in Ni-0.4Cr and Ni0.4Ti, and homogeneous in Ni-0.8Ti and Ni-1.2Ti. These results suggest that the solute addition reduces the heterogeneities of the perfect loop distribution. As the depletion of specific families of perfect loops is probably related to their migration [35], the solute effect on the loop Burgers vector distribution is in line with our conclusions on Ti reducing the loop mobility, presented in Section 3.1.

The unfaulting process of Frank loops depends on the stacking fault energy which is a critical parameter of the alloy. The proportion of faulted and unfaulted loops may be linked to the stacking fault energy of the alloy. Nevertheless, to evaluate this proportion, we need to calculate the total number density of Frank loops and perfect loops including those that escaped from the thin foil. As the probability of formation of the four possible Frank loop sub-families is equal, the density of Frank loops is the simple sum of four sub-families. We assume here perfect loops are formed from the unfaulting of Frank loops and the probability of six possible perfect loop sub-families is equal. Thus, we deduce the total density of perfect loops from the highest sub-family density multiplied by six, to take into account the loss of two sub-families due to their migration towards surfaces. Although in Ni-0.8Ti and Ni-1.2Ti there is no loss of sub-family loops, we rely on the same method to calculate the total perfect loops density in order to keep consistency. Results are presented in Fig. 6(f).

For vacancy-type loops, an addition of Cr reduces the loop density while an addition of Ti increases it. An addition of 0.4 at. % of Ti or Cr slightly increases the ratio Frank loop versus perfect loop. For interstitial loops, an addition of Ti from 0.8 to 1.2 at.% also increase the loop density and the Frank loop proportion. The loop density and the Frank loop proportion between Ni-0.4Ti and Ni-0.8Ti cannot be easily compared as the loop nature change between the two alloys. Therefore, the effect of Ti is consistent for both vacancy-type loops and interstitial-type loops: it increases the Frank loop proportion.

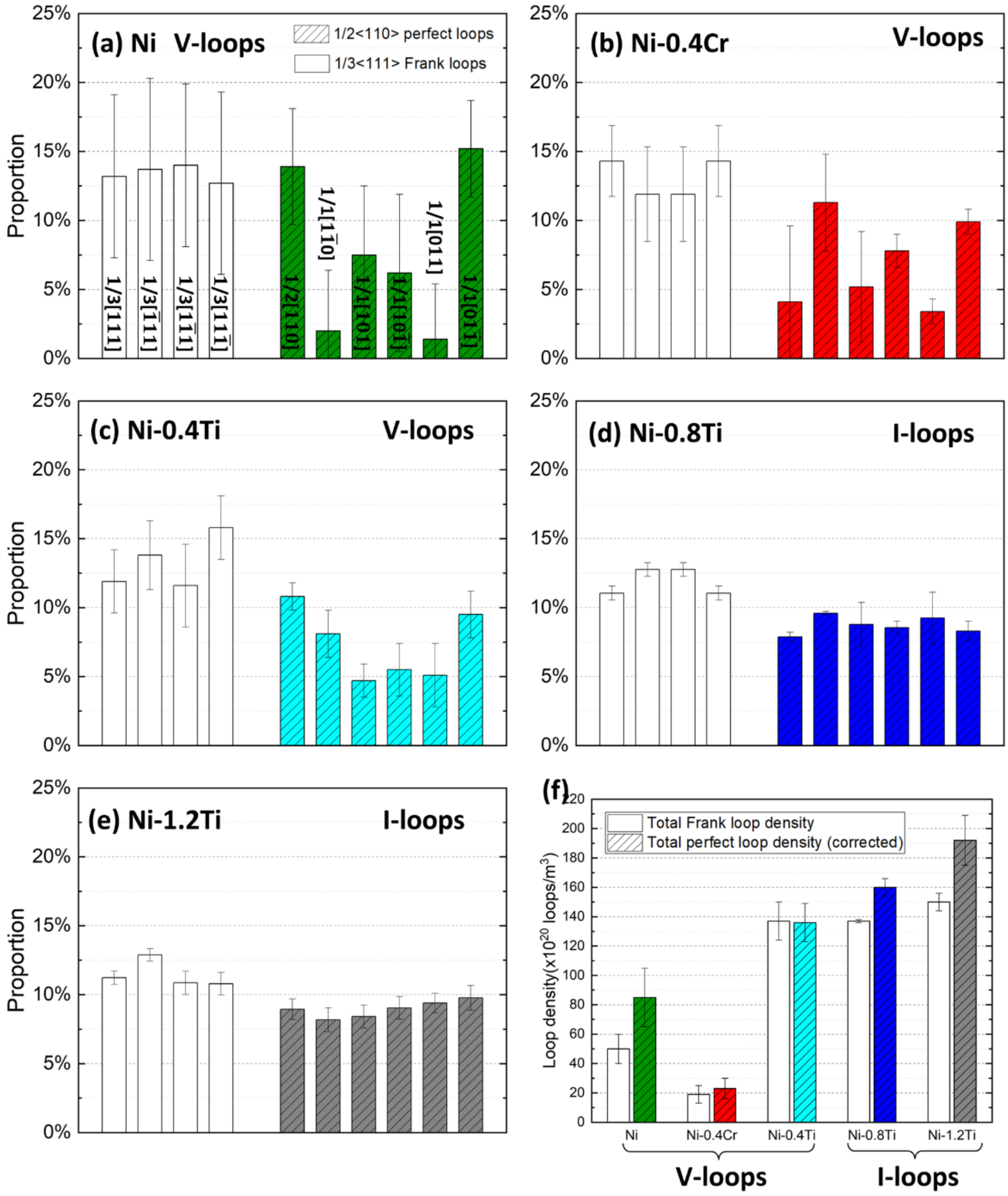

Fig. 6 Proportion of each family of loops calculated by diving the density of each family by the total density in (a) Ni [35], (b) Ni-0.4Cr, (c) Ni-0.4Ti, (d) Ni-0.8Ti and (e) Ni-1.2Ti irradiated at 510°C to 0.06 dpa. Label for each bar giving the loops type shown in (a). (f) Total density of Frank loops and corrected total density of perfect loops (assumed equiprobable) in studied materials with the loop nature indicated as V-loops for vacancy loops and I-loops for interstitial loops..

3.4 Influence of the Ti content and sample thickness on the Frank loop nature at 510°C

The impact of the surfaces is greater the thinner the sample [66]. As the Frank loop nature changes with the Ti content, we expected that the dominating point defect leading to the formation of the dislocation loops is changing as well. Therefore, we investigated the combined effect of the Ti content and the sample thickness on the microstructure. The loops density and average size measured as a function of the specimen thickness are presented in Fig. 7(a) and Fig. 7(b) respectively. The analysis was performed using TEM micrographs shown in Appendix C.

First, the minimum thickness for the observation of loops is 40 nm in Ni-0.8Ti and Ni-1.2Ti and is about 160 nm in pure Ni and Ni-0.4Ti, suggesting less surface effect with 0.8Ti and 1.2Ti. Then, the variation of the loops density with the foil thickness is monotonic for Ni and Ni-0.4Ti whereas for Ni-0.8Ti and Ni-1.2Ti there is a peak in loops density around 100 nm. For most alloys, the loops size increases with increasing thickness. A slight decrease of loops size is observed for Ni at large thicknesses, which is due to the formation of a dislocation network [35]. In relatively thin zones, namely, less than 160 nm, a high density of loops is detected in Ni-0.8Ti and Ni-1.2Ti whereas in Ni and Ni-0.4Ti, only few defects are detected. In Ni-0.8Ti and Ni-1.2Ti, the Frank loops in these thin areas have the same rounded morphology, thereby indicative of the same nature (interstitial-type), as those in thicker zones (see Fig. 6 and Fig. 7(a)). Therefore, the nature of the dislocation loops in Ni-0.8Ti and Ni-1.2Ti alloys is independent of the sample thickness. In relatively thick zones, namely, more than 200 nm, where the influence of the free surfaces in Ni alloys is limited [35], the influence of the Ti content on the loop density and size is not monotonic, as summarized in Table 2, which could be related to the change of loop nature between 0.4 and 0.8 wt.% Ti.

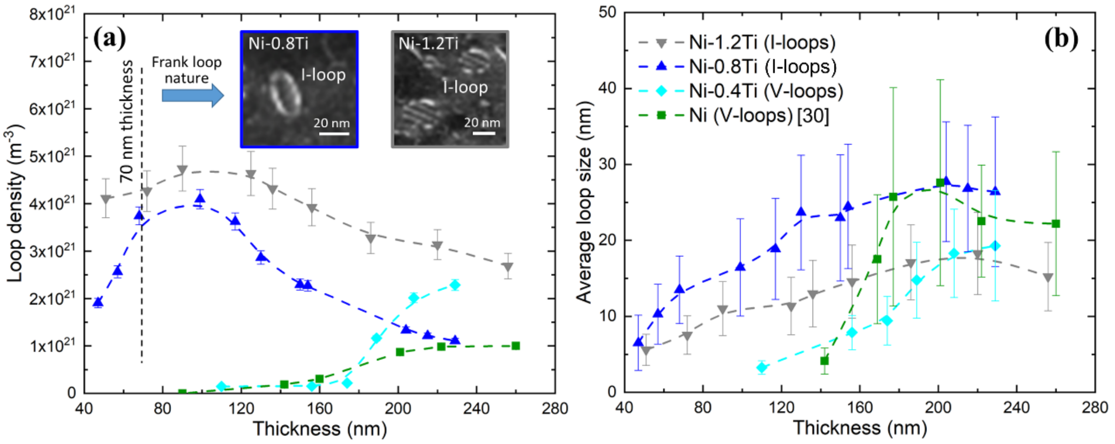

Fig. 7 Sample thickness dependence of the dislocation loops (a) density and (b) average size in Ni [35] and three Ni-Ti alloys irradiated in situ at 510°C to 0.06 dpa. Insets in (a): typical TEM dark field weak beam images of Frank loops in Ni-0.8Ti and Ni-1.2Ti irradiated in situ at 510°C to 0.18 dpa in 70 nm thick zones (higher dose chosen to increase loop size). Labels in (b): "I-loop" denotes interstitial loops and "V-loop" denotes vacancy loops.

Table 2 Variation of Frank dislocation loops density, average size, Frank loop proportion and loop nature as a function of Ti content (wt.%) at 510°C at 0.06 dpa.

Ti content	0	=>	0.4	=>	0.8	=>	1.2
Loop density		↗		Change of loop nature		↗	
Loop size		↘				↘	
Frank loop proportion		↗				↗	
Loop nature		Vacancy-type				Interstitial-type	

These observations allow us to represent schematically the evolution of the dislocation loops microstructure for the same thickness (200 nm) as a function of the Ti content, C_{Ti}, as follows. Globally, with the increase of C_{Ti} the loops density increases while the loops size decreases. However, around the critical concentration of titanium as defined in Section 3.3, which is between 0.4 and 0.8 wt.%, it is difficult to interpret the microstructure evolution with Ti due to the change of loop nature.

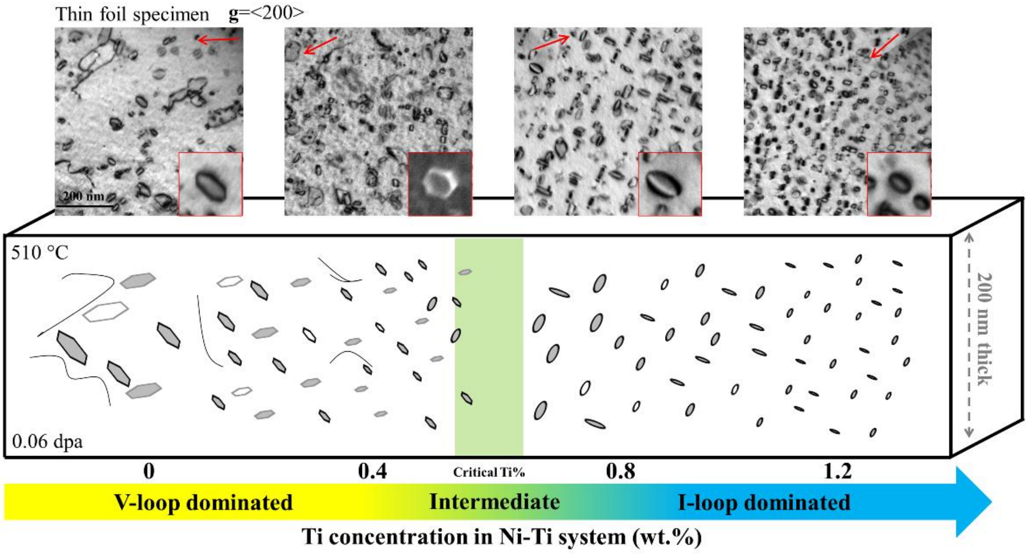

Fig. 8 Schematic representation of the microstructural evolution as a function of Ti content for a specimen thickness around 200 nm. BF TEM micrographs taken with **g**={200} indicated by the red arrow in each micrograph.

3.5 Influence of temperature on the Frank loop nature in thin foil alloys

Finally, it is interesting to investigate the influence of temperature on the Frank loop nature and on the critical Ti concentration, C_{Ti}^{c}. The Frank loops nature was determined in Ni-0.4Cr and Ni-0.4Ti thin foils irradiated at 450°C up to 0.7 dpa (c.f. Appendix D, Fig. D. 1). The analysis is presented in Fig. 9. In Ni and Ni-0.4Cr, Frank loops are vacancy-type at both 510°C and 450°C (Fig. 9(a,b,d,e)), whereas in Ni-0.4Ti, Frank loops are vacancy-type at 510°C (Fig. 9(f)), and interstitial-type at 450°C (Fig. 9(c)). This observation suggests that the critical Ti concentration decreases with temperature or, in another words, that C_{Ti}^{c}(450°C) is lower than 0.4wt.% while C_{Ti}^{c}(510°C) is larger than 0.4 wt.%. The evolution of the Frank loops nature with composition, temperature and sample geometry presented in Fig. 9 is summarized in Table 3.

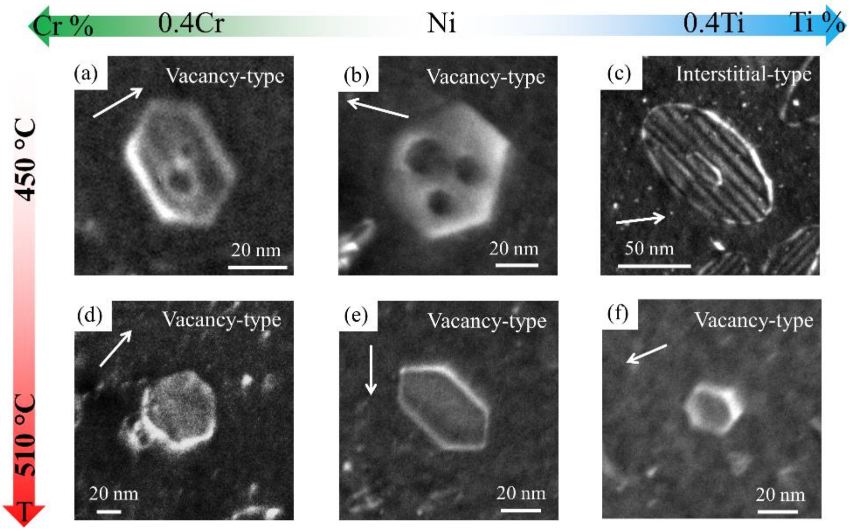

Fig. 9 Typical TEM dark field weak beam image of Frank dislocation loops in thin foils of Ni, Ni-0.4Cr and Ni-0.4Ti as a function of solute type and irradiation temperature. Samples in (a-c) are irradiated at 450°C to 0.7 dpa with 5 MeV Ni^{2+} ions and the ones in (d-f) are irradiated at 510°C to 0.06 dpa with 2 MeV Ni^{2+} ions. Images with **g**={200} indicated by the white arrow in each image.

Table 3. Frank loop nature in function of composition, irradiation temperature and sample geometry

T(°C)	Sample form	Composition				
		Ni	Ni-0.4Cr	Ni-0.4Ti	Ni-0.8Ti	Ni-1.2Ti
510	Thin foil	V-loop [35]	V-loop	V-loop	I-loop	I-loop
450	Thin foil	V-loop [17]	V-loop	I-loop	/	/
450	Bulk	V-loop [17]	I-loop [17]	I-loop [17]	/	/

3.6 Main conclusions on the experimental observations

The main effects of Cr and Ti additions on the radiation-induced dislocation loops microstructure in Ni alloys are the following, starting with the irradiations at 510 °C:

1) A small amount of Ti and Cr reduces the loop mobility and growth rate;
2) Perfect loops glide along their Burgers vector
3) Ti drastically reduces the loop size, but increases the loop density;
4) Free surfaces impact is reduced by the addition of solutes: Frank loops are more numerous and fewer perfect loops are lost while in the irradiation at 450 °C;

5) Dislocation loops are vacancy-type in Ni and Ni-0.4Cr in thin foils at temperature higher than 450°C, while the loop nature in Ni-Ti alloys depends on the Ti content, and temperature. The critical Ti concentration at which there is a switch of the dislocation loop nature depends on the temperature. Above the critical Ti concentration, $C_{Ti}^{c}(T)$, the microstructure is dominated by interstitial loops and below $C_{Ti}^{c}(T)$, loops are vacancy-type. $C_{Ti}^{c}(T)$ decreases with temperature;
6) in Ni-0.8Ti and Ni-1.2Ti (interstitial-loop dominated), the critical thickness for the formation of loop is 40 nm, while in Ni and Ni-0.4Ti (vacancy-loop dominated), it is 160 nm.

4. Discussion

In the following we discuss the underlying mechanisms that could explain the various effects of the solute atoms on the irradiation-induced dislocation loops, and in particular on (i) their mobility, (ii) their growth rate and nature, (iii) the critical sample thickness for their formation, (iv) their number density and (v) the distribution of their Burgers vector. The interplay between solutes and defects arises from thermodynamic interactions and/or from the kinetic coupling between point defects and solutes, which may result in radiation-induced segregation (RIS). We start this chapter with an analysis of RIS, and then analyze the role of the solute-defect thermodynamic interactions based on data obtained by density function theory (DFT) calculations on the loop mobility. From the latter, we model the evolution of the microstructure using rate theory, taking into account these interactions and an effective production bias factor. This allows us to predict the evolution of the dislocation loops properties with respect to temperature, the solute content and the sample thickness as a function of irradiation time.

4.1 Radiation-induced segregation of Ti and Cr in nickel

Radiation-induced segregation (RIS) causes the redistribution of solute atoms in the matrix. In particular, it can lead to their accumulation or their depletion near lattice defects such as the dislocation loops. Recent ab initio calculations show a moderate Ti-vacancy attraction in the nearest neighbor (nn) with a binding energy of 0.05 eV, while with the interstitial it is weaker (0.02 eV) or unstable [67]. Cr presents a relatively weak attraction to the vacancy as 2nd nearest neighbor (2nn) (0.02 eV) while with the interstitial it is stronger (0.1 eV). Hence, we expect a negligible trapping effect of Ti or Cr on PDs.

A quantitative analytical diffusion model has recently been developed to investigate the RIS resulting from the flux of solute atoms towards sinks induced by its coupling with the flux of PDs [68]. The transport coefficients of PDs and solute atoms are obtained from the KineCluE code [69], based on the available PDs jump frequency and migration energy obtained by DFT calculation of Ni-Ti and Ni-Cr alloys [67]. The coupled diffusion equations of PDs and solute are analytically solved to calculate the segregation quantity S_B (B=Ti or Cr) of Ti and Cr in Ni as a function of temperature (K) and damage rate (dpa/s). The segregation amount S_B is defined as the solute concentration excess with respect to the bulk solute concentration. A positive S_B indicates the enrichment at the sink while a negative one indicates depletion. The absolute value of S_B informs about the amplitude of the RIS. To calculate S_B, the total strength of sinks, namely surfaces, dislocation lines, loops and/or voids, of the microstructure is calculated using the formulae given in [70]. The defect number density and size used in the formulae are those experimentally measured in Ni-0.4Ti and Ni-0.4Cr irradiated at 450°C up to 0.7 dpa. As the resulting total sink strength in both alloys is around 10^{14} m^{-2}, we consider in the following that as constant, at the set value of 10^{14} m^{-2}, whatever the temperature and irradiation flux. Although it is a relatively strong approximation, it allows providing a first global picture of the segregation trends in these systems.

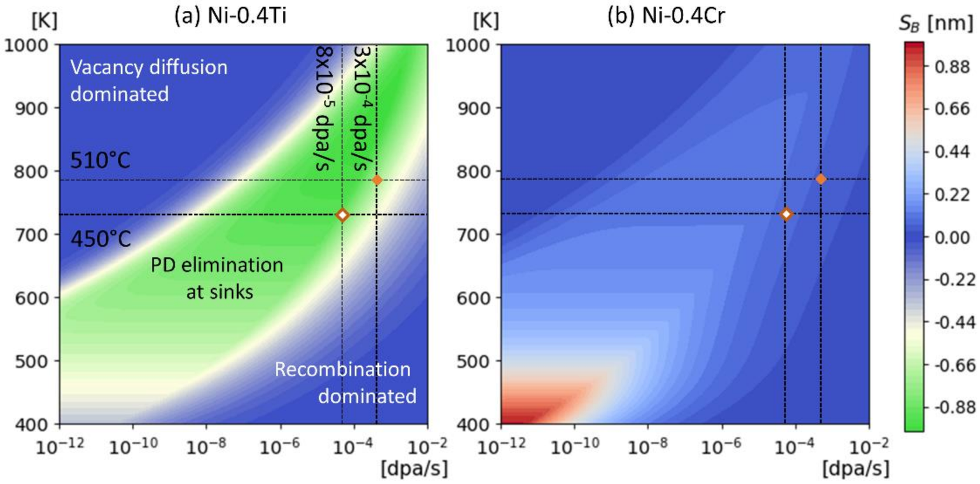

Fig. 10 Radiation-induced segregation (RIS) in (a) Ni-0.4Ti and (b) Ni-0.4Cr systems in function of irradiation temperature and flux calculated by the analytical model [68]. Rhombus indicate the experimental irradiation conditions in this study. Total sink strength used in both systems is set to 10^{14} m^{-2}. The solid rhombus represent in-situ and the hollow ones represent ex-situ irradiation.

Fig. 10 shows the map of the segregation amount, S_B, around a planar sink with the same sink strength as the loops in Ni-0.4Ti and Ni-0.4Cr as a function of irradiation temperature and flux. Both maps show RIS occurs when the mechanism of PD elimination at sinks is dominant in comparison with those of recombination and back diffusion. We observe opposite RIS trends between Ni-Ti and Ni-Cr: sinks are depleted in Ti while they are enriched in Cr. Based on this simulation, within our experiment conditions, we expect Ti depletion to be much more pronounced than the Cr enrichment ($|S_{Ti}| \approx 4|S_{Cr}|$).

Fig. 11 presents the experimental investigation of the solute local distribution in Ni-0.4Ti irradiated at 450°C using STEM-EDS and APT. The STEM HAADF image in Fig. 11a shows a vertical bright contrast that stems from a/2<110> dislocation loops seen edge on. The corresponding STEM EDS maps of Ni and Ti shown in respectively Fig. 11b and c and reveal visually a depletion in Ti at and around the loops, which is also visible in the composition profile taken across loop, see Fig. 11e. There is a dip in the Ti signal when crossing the loop, which corresponds to an increase in the Ni signal, (Fig. 11(e)). Ti depletion around dislocation loops was also recently detected using Atom Probe Tomography (APT) in in the same system, as reported in Fig. 11(f) [71]. At this point no similar investigation has been performed in the Ni-Cr system. Nonetheless, the experimental results in the Ni-Ti confirm our model, which give us confidence in its prediction ability.

The predicted chromium enrichment at dislocation loops could enhance the Cr-dislocation loop interactions, whereas the negative RIS of Ti tends to decrease the interaction between dislocation loops and the population of Ti atoms around them. Both experimental and modeling results show that irradiation leads to a depletion of Ti in the vicinity of defects, which is out of thermal equilibrium segregation. It is worth noting that our experimental study is the first that supports a recent theoretical investigation of flux-couplings in dilute nickel-based alloys predicting negative RIS of Ti and positive RIS of Cr [67].

Despite the radiation-induced depletion of Ti in the vicinity of defects, we observe a spectacular effect of Ti on the dislocation loops mobility and stability. It could be the sign that other mechanisms than RIS, such as thermal segregation, control the defect properties. For example, in austenitic steels, thermodynamics and RIS have opposite effects. RIS induces a depletion of Cr at grain boundaries whereas thermal segregation induces an enrichment. The competition between the two mechanisms leads to a local enrichment of Cr on grain boundaries within a depletion zone. It forms a “w-shape” segregation profile at grain boundary under irradiation [72,73]. However, even if thermodynamics is taking into account in grain boundaries segregation in austenitic steels, it has been underestimated for segregation at radiation-induced dislocation loops. Here, our experimental results may have revealed the crucial role of a thermodynamic driven segregation on the properties of loops, even though the amount of Ti thermal segregation at loops may be too small to be detected. This implies that the thermodynamic interactions of Ti with defects could lead to a thermal segregation of opposite sign to RIS, with a favored occupation of the atomic sites nearby the defect by the solute atoms. We discuss these interactions in more details in the following part.

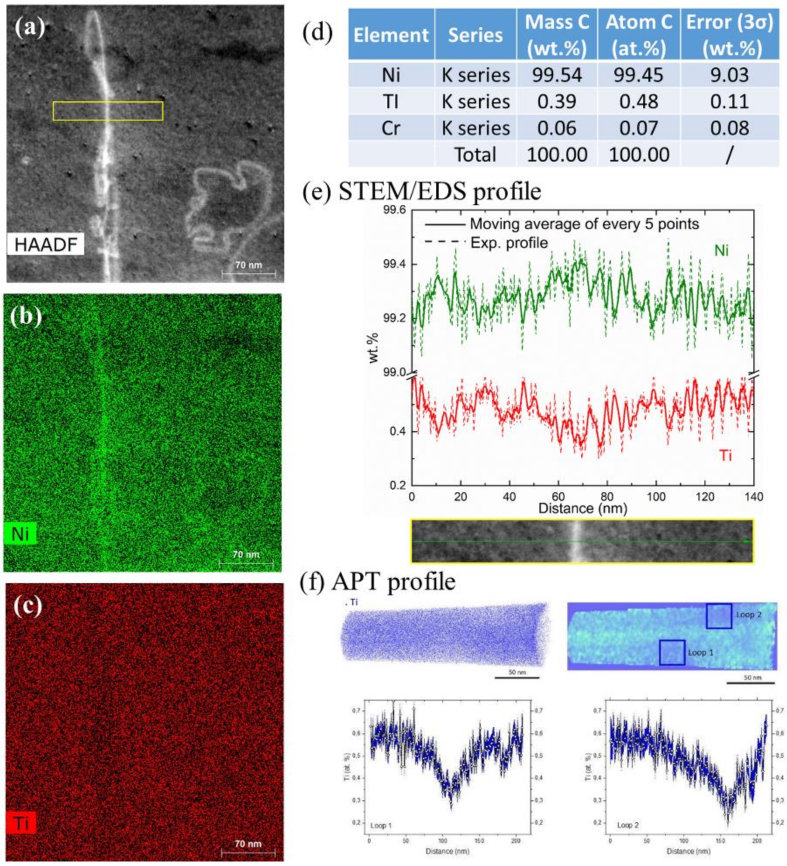

Element	Series	Mass C (wt.%)	Atom C (at.%)	Error (3σ) (wt.%)
Ni	K series	99.54	99.45	9.03
TI	K series	0.39	0.48	0.11
Cr	K series	0.06	0.07	0.08
	Total	100.00	100.00	/

Fig. 11 (a) STEM-HAADF image and STEM EDS map of (b) Ni and (c) Ti of Ni-0.4Ti irradiated at 450°C to 0.7 dpa. Region contains one dislocation loop in edge-on position (vertical bright contrast in (a)); (d) overall composition of the imaged zone; (e) concentration profile of Ti and Ni across the dislocation loop taken in the yellow box marked in (a). (f) APT and APT profile showing Ti depletion at dislocation loops (from [71]).

4.2 Thermodynamic solute-defect interactions

The loop mobility in concentrated Ni alloys was observed to be lower than in pure Ni under irradiation [43,47]. The reduced mobility was attributed to the strong lattice distortion induced by the addition of a high amount of solute. In the present study, although alloys are dilute in solute, we still observe a strong reduction of the loop mobility (Fig. 6), especially in Ni-Ti, likely due to the thermal segregation of Ti as we suggested above. Unfortunately, a direct observation of a solute thermal segregation on radiation-induced defects is difficult to achieve, because the amount and the spatial extent of a thermal segregation may be below the spatial and chemical resolution of STEM EDS and of APT. However, atomistic modeling studies provide elements of answer: recent *ab initio* studies indicate that the standard elastic models correctly predict the sign of thermal solute segregation on dislocation lines and interstitial dislocation loops [52,53]. It was shown that there is a direct relationship between the solute-dislocation loop binding energy and the relaxation volume of the solute in the matrix. In order to minimize the energy of system, a solute larger than the matrix atoms preferentially resides in tensile regions and, vice versa, a small solute preferentially resides in compressive regions. Around a dislocation loop, whatever its nature (vacancy or interstitial), there are tensile and compressive regions. Therefore, one can always expect an enrichment of solute nearby loops, as long as the solute relaxation volume is non-zero, whatever its sign. In Ni, the relaxation volume of Ti is positive, while it is slightly negative for Cr [74,75]. We thus expect a smaller elastic interaction of Cr with defects compared to Ti. Note that voids and stacking fault tetrahedra generate smaller distortions of the surrounding lattice compared to dislocation loops.

Electronic interactions may compete with elastic interactions, especially when the elastic interactions are small. While there is no systematic *ab initio* analysis of the Cr and Ti interactions with the various defects at play, some recent ab initio studies revealed a lowering of the stacking fault energy resulting from a shear deformation along <112>{111} upon the substitution of Ni by either Ti and Cr [75]. In a first approach, we considered I-clusters, Frank loops and stacking fault tetrahedra as defects generating stacking faults. We may thus conclude that Ti and Cr solutes are certainly attracted to these defects.

To conclude, we expect Ti, and Cr to a lesser extent, to be attracted to both interstitial and vacancy dislocation loops, and stacking fault tetrahedra and I-clusters. This attraction results from a purely thermodynamic effect, leading to local solute enrichments close to those defects. In the case of Cr, we predict a slightly positive RIS at defects, as shown in Fig. 10(b). When there is a thermodynamic Cr-defect attraction, the radiation-induced enrichment of Cr may enhance the attraction of Cr with the defects, which means in particular that the dislocation loop mobility will be more impacted by Cr. In the case of Ti, the thermal segregation of Ti nearby loops against the Ti depletion by RIS may play a key role on the loop mobility and stability. However, to predict such a fine thermal segregation, further investigations such as interaction between Ti and dislocation core are required.

Note that, in concentrated alloys, thermal segregation occurs as well, but it is then not necessarily the dominant phenomenon impacting the mobility of dislocations. For instance, one has demonstrated the strong role of bulk composition fluctuations on the dislocation mobility [76]. The opposite sign of radiation induced and assumed thermal segregation in Ni-Ti tends to show that the dislocation mobility is mainly sensitive to equilibrium segregation rather than to non-equilibrium segregation.

4.3 From the slowing down of PD clusters by solutes to the growth rate and nature of the dislocation loops

In most alloys, the solute segregation at defect delays the defect mobility. Indeed, whenever the motion of defect proceeds via a dissociation reaction of the solute from the PD cluster, the activation barrier of the PD cluster motion increases with the solute-PD cluster binding energy and the amount of segregated solute atoms. Therefore, the greater the segregation, the slower the motion of PD clusters. The amount of segregation relates to the interplay between the solute atoms and the loops growth rate and nature.

To understand the solutes effect on the loops growth rate and nature, we applied rate theory, considering the production bias model [35] to account for the loss of freely migrating interstitial resulting from their diffusion and elimination at the free surfaces of the sample. In our previous investigation [35], this model could explain the growth of vacancy loops in Ni. The steady-state variation of the vacancy (v) loop radius, R, is written as:

$\frac{dR}{dt} = \alpha(1-\eta) + \beta$ Equation (1) [35]

where $\alpha(1-\eta)$ describes the loss of interstitials due to the migration of PD clusters and β is the loop growth rate based on the standard dislocation bias and PD diffusion models [22,36,37]. The expressions of α and β are given in Appendix E. We define here a critical loss $(1-\eta_c)$ which makes $\alpha(1-\eta_c) + \beta = 0$. When the interstitial loss is higher than the critical loss, i.e. $(1-\eta) > (1-\eta_c)$, the sum on the right side of Eq.(1) is positive so vacancy loops grow. Otherwise, interstitial loops grow. We discuss below the impact of the SIA loss or lack thereof resulting from the action of solute on the PD cluster mobility on the loop nature and growth.

The impact of solute atoms on the loop nature and growth rate may relate to the suppression of the interstitial loss in their presence. The thermal segregation of solutes would reduce the interstitial cluster (I-cluster) mobility, thus reduce the interstitial loss mediated by the mobility and elimination reactions of I-clusters. In Ni-Ti alloys, the increase of Ti thermal segregation with the nominal concentration of Ti, should lead to a progressive decrease of the loop and cluster mobilities, thus progressive decrease of the production bias, $(1-\eta)$. Following Eq. (1), the growth rate of vacancy loops decreases with a decrease of the production bias. Once Ti content exceeds a critical value, the sign of the growth rate changes, implying a change of the loop nature with the nominal Ti content.

Table 4 summarizes the main findings resulting for this modelling. Based on Eq. (1) and the measurement of the loop growth rate, we may obtain a quantitative estimation of the interstitial loss rate. Using the measured growth rate dR/dt (Fig. 2(c) with values given in Appendix E), and the evaluation of the sink strength extracted from the experimental characterization of the overall dislocation microstructure (Appendix E), the interstitial loss rate was estimated by solving the Equation (1) c.f. Table 4. The loop growth rate and irradiated microstructure data are the ones measured at the end of irradiation. In vacancy loop dominated materials, the interstitial loss is higher than the critical loss, which is reached when dR/dt=0 in Equation (1), while in interstitial loop dominated ones, it is below the critical value.

Table 4 Minimum interstitial loss (critical loss) to induce vacancy loop growth and estimated interstitial loss deduced from observed loop growth rate at the end irradiation based on rate theory model [35] in materials irradiated at 510°C up to 0.06 dpa.

Materials	Ni	Ni-0.4Cr	Ni-0.4Ti	Ni-0.8Ti	Ni-1.2Ti

Loop nature	V-loop	V-loop	V-loop	I-loop	I-loop
Thickness (nm)	260	220	220	120	120
Critical loss	~7%	~7%	~7%	~9%	~9%
Estimated loss	~12%	~16%	~10%	~7%	~6%

Table 4 gives the Frank loop nature in function of composition, temperature and the sample thickness. The micro-alloying, the decrease of temperature c.f. Table 3 (reducing the cluster mobility), the increase of the sample thickness (from TEM thin foil to bulk), and the increase of the solute content lead in general, to a lower interstitial loss. This is an indirect proof of their impact on the nature of the dislocation loops and their mobility. Besides, the effect of Ti on the defect mobility is stronger than the one of Cr. In Ni-0.4Cr thin foil at both 510°C and 450°C, the mobility of I-cluster is reduced but not enough to reverse the loop nature because the interstitial loss to surfaces remains strong despite the microalloying. In bulk Ni-0.4Cr, the interstitial loss is largely reduced in depth, up to the formation of a dislocation-loop population dominated by I-loops.

4.4 Critical sample thickness for the formation of loops, dependence on cluster mobility and stability

The critical thickness at which we observe loops is different between vacancy-loop-dominated samples and interstitial-loop-dominated samples (c.f. Fig. 7). In pure Ni [35] and Ni-0.4Ti at 510°C, (vacancy-type) dislocation loops are present at thickness above 150 nm (c.f. Fig. 7(a)). In Ni-0.8Ti and Ni-1.2Ti, (interstitial-type) dislocation loops are observed already at thicknesses as low as 40 nm (c.f. Fig. 7(b)). More specifically, in Ni (450&510°C) and Ni-0.4Ti (510°C) I-defects are more mobile than V-defects as shown in Fig. 12(a). I-defects can thus easily escape to surfaces whatever the thickness. In thin zones, there is no vacancy loop as both types of clusters are strongly absorbed at the free surfaces. An increase of the thickness leads to an increase of the vacancy concentration, leading to the formation of vacancy dislocation loops. In Ni-0.4Ti (450°C) and Ni-0.8Ti and Ni-1.2Ti (510°C), a loop-free thin zone (below 40 nm) is observed where both I-defects and V-defects are absent due to the strong elimination rate at surfaces. As the thickness increases, a part of the loops formed within the cascades, survive. In Ni-0.8Ti and Ni-1.2Ti, as loops are immobile and have stronger bias than any other sinks (surface, voids and stacking fault tetrahedra (SFT), I-loops would strongly attract I-defects and grow while V-loops would shrink (see Fig. 12(b)).

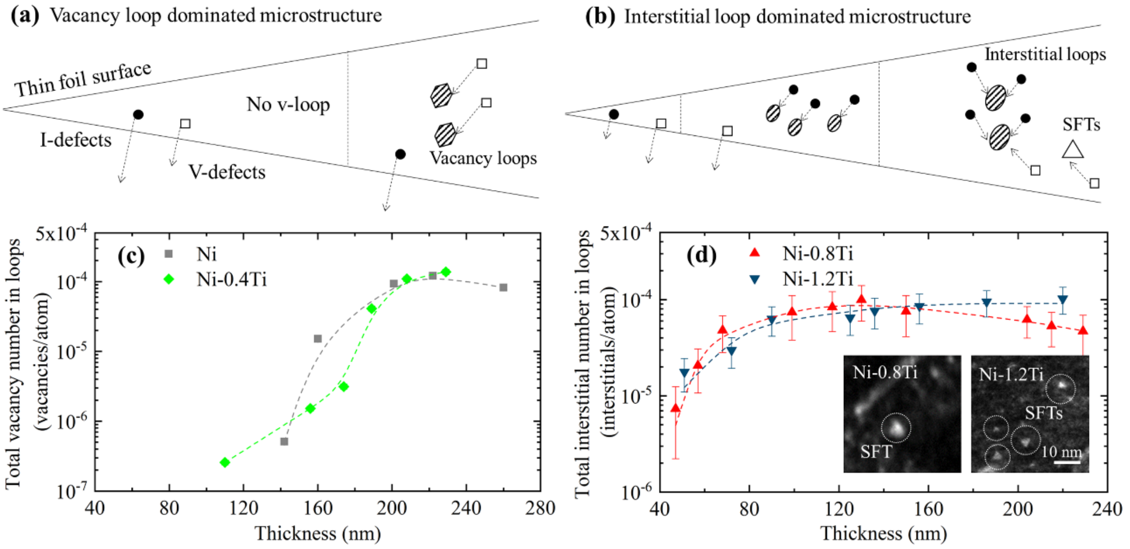

Fig. 12 Schematic illustration for the loop formation in irradiated lean Ni alloys in respectively (a) a vacancy loop-dominated material and (b) an interstitial loop-dominated material. (c) Total vacancy number contained in loops as a function of thickness in Ni and Ni-0.4Ti up to 0.06 dpa; (d) total interstitial number contained in loops in Ni-0.8Ti and Ni-1.2Ti irradiated at 510°C up to 0.18 dpa. TEM micrographs in (d) taken in dark-field weak-beam mode.

The difference in the loops nature between Ni-0.8/1.2Ti and Ni/Ni-0.4Ti could be attributed to the variation of the radiation dose. However, during the in-situ irradiation, the morphology of the Frank loops remained the same in each material, which indicates that no change of the loops nature took place within the studied dose range.

To support this conclusion, the total PD number (either vacancy number or interstitial number) contained in loops is estimated as explained in Appendix F. The total vacancy number contained in loops in Ni and Ni-0.4Ti and the total interstitial number in

Ni-0.8Ti and Ni-1.2Ti at 510°C are calculated as a function of the sample thickness. They are presented in respectively Fig. 12(c) and Fig. 12(d). These curves show a good agreement with the suggested mechanism drawn from Fig. 12(a) and Fig. 12(b).

It is worth noting that stacking fault tetrahedra (SFT) were detected in our samples (see. Fig. 12(d)). It is however difficult to determine their size and number density, as they are usually at the limit of the spatial resolution of TEM imaging in diffraction contrast mode (about half a nanometer), which also renders the identification of their shape difficult. However, SFTs are more frequently and easily observed in Ni-0.8/1.2Ti than in Ni/Ni-0.4Ti, as their density and size seem to increase with the Ti content. DFT calculations have shown that Ti could efficiently reduce the stacking fault energy (SFE) in nickel [75,77], which implies that the SFT is energetically more favourable with increasing Ti content.

4.5 Loop mobility and stability impacting loop density

The overall loops density is increased by Ti (c.f. Fig. 6). Two mechanisms involving Ti solute may operate. First, the nucleation of Frank loops may be enhanced by the reduction of the SFE with the Ti concentration increase. It would lead to a higher Frank loops density, which in turn would also increase the number of perfect loops, as Frank loops unfault into perfect loops during the loop growth. This hints towards the influence of solute on the unfaulting process or critical unfaulting size, which is beyond the scope of this work. The second mechanism concerning the loop mobility has been discussed previously: the mobility of perfect loops is reduced in Ni-Ti alloys, likely due to the thermal Ti segregation. This trapping effect reduces the number of perfect loops slipping to surfaces and hence the heterogeneities in the Burgers vector distribution of the perfect dislocation loops. The effect of Cr on the loop density is not strong, probably due to the fact that Cr moderately affects the SFE [75,77] and loop mobility (Table 1).

5. Conclusion

In-situ and ex-situ self-ion irradiations and fine analysis of irradiated microstructure are performed on dilute Ni-based model alloys to investigate the influence of micro-alloying on the radiation damage of fcc alloys. Our results show that:

1) The influence of three parameters (solute nature, solute concentration and temperature) on the dislocation-loop nature (interstitial vs vacancy) of the fcc nickel structure is revealed for the first time. The influence of micro-alloying on the dislocation loop microstructure strongly depends on the nature of the solute element. Titanium has a strong effect on various properties of dislocation loops, including their nature, their growth rate, their density, their Burgers vector and their mobility, while the effect of chromium appears as moderate. The strong effects of Ti micro-alloying on the loop mobility, the loop growth rate and loop nature are attributed to the slowing down of clusters, likely due to the thermal segregation of this oversized solute atom at radiation-induced defects. This thermodynamic effect depends on the solute content and temperature, which is consistent with our experimental observations. The critical Ti concentration at which there is a switch of the dislocation loop nature depends on the temperature. Above the critical Ti concentration, $C_{Ti}^{c}(T)$, the microstructure is dominated by interstitial loops and below $C_{Ti}^{c}(T)$, loops are vacancy-type. $C_{Ti}^{c}(T)$ decreases with temperature.

2) We demonstrate that in alloys, there is a direct correlation between the Frank loop morphology and their nature. Vacancy Frank loops show a segmented shape while interstitial ones are ellipsoidal.
3) The addition of solute reduces the critical thickness for the formation of loops. Interstitial-type loops form at thickness above 40 nm while vacancy-type loops form at thickness above 150 nm. We attribute such critical regimes to the reduced mobility of I-clusters.
4) An addition of titanium reduces the mobility of loops and the stacking fault energy of nickel. The impact of Ti on the stacking fault energy is evidenced by the increase of both Frank loop proportion and stacking fault tetrahedra size/density with the addition of Ti in the alloys. This observations confirms the previous DFT calculations.
5) Under the studied conditions (450°C and $8x10^{-5}$ dpa/s), a depletion of Ti could be detected using STEM/EDS and APT. We have deployed a new radiation-induced segregation (RIS) model based on experimental evidence and recent DFT-KineCluE modeling of RIS accounting for the effect of the overall microstructure sink strength (characterized by TEM) on the amount of segregation. The coupling of experiments and modelling reveals that radiation-induced segregation (RIS) leads to a depletion of Ti nearby defects under irradiation. Our experimental study is indeed the first that supports recent DFT theoretical calculations highlighting the variety of flux-coupling mechanisms in dilute nickel-based alloys.
6) Based on DFT data and our experimental observations, we attribute the observed spectacular solute effects of Ti on loop nature and growth to the thermal segregation of oversized Ti atoms at strained lattice sites of the defects. The

opposite sign of RIS and thermal segregation in Ni-Ti suggests that the dislocation mobility is mainly sensitive to equilibrium segregation rather than to non-equilibrium segregation. This interpretation including thermodynamics sheds new light on the underlying fundamental mechanisms of the influence of micro-alloying on radiation damage. This opens new perspectives for future experimental investigations and for the development of the modeling of radiation effects.

Declaration of Competing Interests

The authors declare that they have no known competing financial interests or personal relationships that could have appeared to influence the work reported in this paper.

Acknowledgement

The research was supported by the Cross-cutting basic research Program of Division Energy of CEA (RTA Program), the RMATE project (CEA), the NEEDS program (CNRS-CEA-EDF-ANDRA-AREVA-IRSN-BRGM), and by the French government, managed by the French National Research Agency, under the “Investissements d'avenir” program (No. ANR-11-EQPX-0020). These experiments were supported by the French EMIR&A accelerators network. The authors are grateful to the JANNuS-Saclay team for performing ex-situ irradiation and to the JANNuS-Orsay/SCALP technical staff at IJCLab (formerly CSNSM) for ARAMIS ion irradiations, and technical help at the TEM during in-situ experiments, especially Cédric Baumier, Jérôme Bourçois, Sandrine Picard, and Cyril Bachelet. Kan Ma and Marie Loyer-Prost acknowledge the inspiring discussion on mechanisms with Thomas Jourdan in SRMP/CEA-Saclay.

Reference

[1] P. Yvon, Structural Materials for Generation IV Nuclear Reactors, 1st ed., Woodhead Publishing, United Kingdoms, 2016.

[2] F.A. Garner, Radiation Damage in Austenitic Steels, in: Comprehensive Nuclear Materials, Elsevier, 2012: pp. 33–95. https://doi.org/10.1016/B978-0-08-056033-5.00065-3.

[3] G.S. Was, Fundamentals of Radiation Materials Science: Metals and Alloys, Springer, 2016.

[4] F. Garner, H. Brager, Swelling of Austenitic Iron-Nickel-Chromium Ternary Alloys During Fast Neutron Irradiation, in: F. Garner, J. Perrin (Eds.), Effects of Radiation on Materials: Twelfth International Symposium, ASTM International, 100 Barr Harbor Drive, PO Box C700, West Conshohocken, PA 19428-2959, 1985: pp. 187-187–15. https://doi.org/10.1520/STP37361S.

[5] F.A. Garner, H.R. Brager, R.J. Puigh, Swelling behavior of titanium-modified alloys in EBR-II, Journal of Nuclear Materials. 133–134 (1985) 535–539. https://doi.org/10.1016/0022-3115(85)90205-3.

[6] W.G. Johnston, J.H. Rosolowski, A.M. Turkalo, T. Lauritzen, An experimental survey of swelling in commercial Fe-Cr-Ni alloys bombarded with 5 MeV Ni Ions, Journal of Nuclear Materials. 54 (1974) 24–40. https://doi.org/10.1016/0022-3115(74)90073-7.

[7] J.F. Bates, R.W. Powell, Irradiation-induced swelling in commercial alloys, Journal of Nuclear Materials. 102 (1981) 200–213. https://doi.org/10.1016/0022-3115(81)90560-2.

[8] E.H. Lee, A.F. Rowcliffe, E.A. Kenik, Effects of Si and Ti on the phase stability and swelling behavior of AISI 316 stainless steel, Journal of Nuclear Materials. 83 (1979) 79–89. https://doi.org/10.1016/0022-3115(79)90594-4.

[9] T. Muroga, K. Araki, Y. Miyamoto, N. Yoshida, Void swelling in high purity Fe-Cr-Ni and Fe-Cr-Ni-Ti alloys irradiated in JOYO, Journal of Nuclear Materials. 155–157 (1988) 1118–1122. https://doi.org/10.1016/0022-3115(88)90479-5.

[10] N. Sekimura, S. Ishino, The effect of titanium addition on microstructural evolution in austenitic steel irradiated with fast neutrons in FFTF, Journal of Nuclear Materials. 179–181 (1991) 542–545. https://doi.org/10.1016/0022-3115(91)90145-W.

[11] C. David, B.K. Panigrahi, S. Balaji, A.K. Balamurugan, K.G.M. Nair, G. Amarendra, C.S. Sundar, B. Raj, A study of the effect of titanium on the void swelling behavior of D9 steels by ion beam simulation, Journal of Nuclear Materials. 383 (2008) 132–136. https://doi.org/10.1016/j.jnucmat.2008.08.049.

[12] E. Meslin, M. Lambrecht, M. Hernández-Mayoral, F. Bergner, L. Malerba, P. Pareige, B. Radiguet, A. Barbu, D. Gómez-Briceño, A. Ulbricht, Characterization of neutron-irradiated ferritic model alloys and a RPV steel from combined APT, SANS, TEM and PAS analyses, Journal of Nuclear Materials. 406 (2010) 73–83.

[13] A. Bhattacharya, E. Meslin, J. Henry, A. Barbu, S. Poissonnet, B. Décamps, Effect of chromium on void swelling in ion irradiated high purity Fe–Cr alloys, Acta Materialia. 108 (2016) 241–251. https://doi.org/10.1016/j.actamat.2016.02.027.

[14] M. Matijasevic, A. Almazouzi, Effect of Cr on the mechanical properties and microstructure of Fe–Cr model alloys after n-irradiation, Journal of Nuclear Materials. 377 (2008) 147–154.

[15] F. Soisson, T. Jourdan, Radiation-accelerated precipitation in Fe–Cr alloys, Acta Materialia. 103 (2016) 870–881.

[16] S.I. Porollo, A.M. Dvoriashin, Yu.V. Konobeev, F.A. Garner, Microstructure and swelling of neutron irradiated nickel and binary nickel alloys, Journal of Nuclear Materials. 442 (2013) S809–S812. https://doi.org/10.1016/j.jnucmat.2013.05.019.

[17] K. Ma, B. Décamps, A. Fraczkiewicz, F. Prima, M. Loyer-Prost, Drastic influence of micro-alloying on Frank loop nature in Ni and Ni-based model alloys, Materials Research Letters. 8 (2020) 201–207. https://doi.org/10.1080/21663831.2020.1741042.

[18] J. Koger, Evaluation of Hastelloy N alloys after nine years exposure to both a molten fluoride salt and air at temperatures from 700 to 560 0 C, Oak Ridge National Lab., 1972.

[19] T. Yoshiie, Q. Xu, Y. Satoh, H. Ohkubo, M. Kiritani, The effect of alloying elements on the defect structural evolution in neutron irradiated Ni alloys, Journal of Nuclear Materials. 283–287 (2000) 229–233.

[20] S.J. Zinkle, L.L. Snead, Microstructure of copper and nickel irradiated with fission neutrons near 230°C, Journal of Nuclear Materials. 225 (1995) 123–131. https://doi.org/10.1016/0022-3115(94)00670-9.

[21] J.L. Brimhall, B. Mastel, Voids in neutron irradiated face centered cubic metals, Journal of Nuclear Materials. 29 (1969) 123–125. https://doi.org/10.1016/0022-3115(69)90132-9.

[22] M. Kiritani, N. Yoshida, H. Takata, Y. Maehara, Growth of Interstitial Type Dislocation Loops and Vacancy Mobility in Electron Irradiated Metals, Journal of the Physical Society of Japan. 38 (1975) 1677–1686. https://doi.org/10.1143/JPSJ.38.1677.

[23] K. Urban, Growth of defect clusters in thin nickel foils during electron irradiation (I), Physica Status Solidi (a). 4 (1971) 761–772. https://doi.org/10.1002/pssa.2210040321.

[24] M.H. Yoo, J.O. Stiegler, Growth kinetics and ‘preference factor’ of Frank loops in nickel during electron irradiation, Philosophical Magazine. 36 (1977) 1305–1315. https://doi.org/10.1080/14786437708238518.

[25] R.F. Pinizzotto, L.J. Chen, A.J. Ardell, Nickel and nitrogen ion irradiation induced void swelling and defect microstructures in Ni-Al, Ni-Cr and Ni-Ti solid solutions, Metallurgical Transactions A. 9 (1978) 1715–1727. https://doi.org/10.1007/BF02663401.

[26] L.J. Chen, A.J. Ardell, The observation of multiple-layer loops in nickel base alloys under ion bombardment, Physica Status Solidi (a). 34 (1976) 679–690. https://doi.org/10.1002/pssa.2210340232.

[27] D.J. Mazey, J.A. Hudson, Observation of large faulted interstitial loops in proton-irradiated nickel, Journal of Nuclear Materials. 37 (1970) 13–17.

[28] D.I.R. Norris, Dislocation loop growth in an electron irradiated thin foil, Philosophical Magazine. 22 (1970) 1273–1278. https://doi.org/10.1080/14786437008226935.

[29] S. Ishino, K. Fukuya, T. Muroga, N. Skinura, H. Kawanishi, In-situ microstructural observation of radiation damage in nickel produced by energetic heavy particles, Journal of Nuclear Materials. 122 & 123 (1984) 597–601.

[30] T.M. Robinson, M.L. Jenkins, Heavy-ion irradiation of nickel and nickel alloys, Philosophical Magazine A. 43 (1981) 999–1015. https://doi.org/10.1080/01418618108239507.

[31] C. Lu, K. Jin, L.K. Béland, F. Zhang, T. Yang, L. Qiao, Y. Zhang, H. Bei, H.M. Christen, R.E. Stoller, L. Wang, Direct Observation of Defect Range and Evolution in Ion-Irradiated Single Crystalline Ni and Ni Binary Alloys, Scientific Reports. 6 (2016). https://doi.org/10.1038/srep19994.

[32] H.C. Chen, R.D. Lui, C.L. Ren, H.F. Huang, J.J. Li, G.H. Lei, W.D. Xue, W.X. Wang, Q. Huang, D.H. Li, L. Yan, X.T. Zhou, Evolution of dislocation loops in He ion irradiated nickel under different temperature, Journal of Applied Physics. 120 (2016) 125303. https://doi.org/10.1063/1.4963344.

[33] R. Schäublin*, Z. Yao, N. Baluc, M. Victoria, Irradiation-induced stacking fault tetrahedra in fcc metals, Philosophical Magazine. 85 (2005) 769–777.

[34] R. Schibli, R. Schäublin, On the formation of stacking fault tetrahedra in irradiated austenitic stainless steels – A literature review, Journal of Nuclear Materials. 442 (2013) S761–S767. https://doi.org/10.1016/j.jnucmat.2013.05.077.

[35] K. Ma, B. Décamps, A. Fraczkiewicz, T. Jourdan, F. Prima, M. Loyer-Prost, Free surface impact on radiation damage in pure nickel by in-situ self-ion irradiation: can it be avoided?, Acta Materialia. 212 (2021) 116874. https://doi.org/10.1016/j.actamat.2021.116874.

[36] A.D. Brailsford, R. Bullough, The rate theory of swelling due to void growth in irradiated metals, Journal of Nuclear Materials. 44 (1972) 121–135. https://doi.org/10.1016/0022-3115(72)90091-8.

[37] J.E. Harbottle, D.I.R. Norris, High voltage electron microscope studies of void nucleation in nickel, Journal of Microscopy. 97 (1973) 129–138. https://doi.org/10.1111/j.1365-2818.1973.tb03767.x.

[38] R. Bullough, M.H. Wood, D.W. Wells, J.R. Willis, The interaction energy between interstitial atoms and dislocation and its relevance to irradiation damage process, in: Dislocation Modelling of Physical Systems, Pergamon, 1981: pp. 116–141. https://doi.org/10.1016/B978-0-08-026724-1.50017-0.

[39] D. Carpentier, Simulation de la cinétique d’absorption des défauts ponctuels par les dislocations et amas de défauts, Ph.D. thesis, Université Paris-Saclay, 2018. https://pastel.archives-ouvertes.fr/tel-01915303/document.

[40] D. Carpentier, T. Jourdan, Y. Le Bouar, M.-C. Marinica, Effect of saddle point anisotropy of point defects on their absorption by dislocations and cavities, Acta Materialia. 136 (2017) 323–334.

[41] C.H. Woo, B.N. Singh, Production bias due to clustering of point defects in irradiation-induced cascades, Philosophical Magazine A. 65 (1992) 889–912. https://doi.org/10.1080/01418619208205596.

[42] N. Doan, D. Rodney, G. Martin, Interstitial cluster motion in nickel: a molecular dynamics study, in: Trans Tech Publ, 2001: pp. 43–48.

[43] C. Lu, L. Niu, N. Chen, K. Jin, T. Yang, P. Xiu, Y. Zhang, F. Gao, H. Bei, S. Shi, M.-R. He, I.M. Robertson, W.J. Weber, L. Wang, Enhancing radiation tolerance by controlling defect mobility and migration pathways in multicomponent single-phase alloys, Nature Communications. 7 (2016) 13564. https://doi.org/10.1038/ncomms13564.

[44] E. Wakai, T. Ezawa, J. Imamura, T. Takenaka, T. Tanabe, R. Oshima, Effect of solute atoms on swelling in Ni alloys and pure Ni under He+ ion irradiation, Journal of Nuclear Materials. (2002) 7.

[45] Y. Zhang, G.M. Stocks, K. Jin, C. Lu, H. Bei, B.C. Sales, L. Wang, L.K. Béland, R.E. Stoller, G.D. Samolyuk, Influence of chemical disorder on energy dissipation and defect evolution in concentrated solid solution alloys, Nature Communications. 6 (2015) 1–9.

[46] C. Dimitrov, O. Dimitrov, Composition dependence of defect properties in electron-irradiated Fe-Cr-Ni solid solutions, Journal of Physics F: Metal Physics. 14 (1984) 793.

[47] C. Lu, T. Yang, L. Niu, Q. Peng, K. Jin, M.L. Crespillo, G. Velisa, H. Xue, F. Zhang, P. Xiu, Interstitial migration behavior and defect evolution in ion irradiated pure nickel and Ni-xFe binary alloys, Journal of Nuclear Materials. 509 (2018) 237–244.

[48] L. Wang, R. Dodd, G. Kulcinski, Effects of 14 MeV nickel ion irradiation on nickel-copper alloys observed in cross-section, Journal of Nuclear Materials. 155 (1988) 1241–1248.

[49] L. Wang, S. Zinkle, R. Dodd, G. Kulcinski, Effects of preinjected helium in heavy-ion irradiated nickel and nickel-copper alloys, Metallurgical Transactions A. 21 (1990) 1847–1851.

[50] J.R. Manning, Correlation factors for diffusion in nondilute alloys, Physical Review B. 4 (1971) 1111.

[51] K.C. Russell, Phase stability under irradiation, Progress in Materials Science. 28 (1984) 229–434. https://doi.org/10.1016/0079-6425(84)90001-X.

[52] R.C. Birtcher, M.A. Kirk, K. Furuya, G.R. Lumpkin, M.-O. Ruault, In situ Transmission Electron Microscopy Investigation of Radiation Effects, Journal of Materials Research. 20 (2005) 1654–1683. https://doi.org/10.1557/JMR.2005.0242.

[53] M. Suzuki, A. Sato, T. Mori, J. Nagakawa, N. Yamamoto, H. Shiraishi, In situ deformation and unfaulting of interstitial loops in proton-irradiated steels, Philosophical Magazine A. 65 (1992) 1309–1326.

[54] D. Brimbal, B. Décamps, J. Henry, E. Meslin, A. Barbu, Single- and dual-beam in situ irradiations of high-purity iron in a transmission electron microscope: Effects of heavy ion irradiation and helium injection, Acta Materialia. 64 (2014) 391–401. https://doi.org/10.1016/j.actamat.2013.10.052.

[55] X. Yi, M.L. Jenkins, M.A. Kirk, Z. Zhou, S.G. Roberts, In-situ TEM studies of 150 keV W+ ion irradiated W and W-alloys: Damage production and microstructural evolution, Acta Materialia. 112 (2016) 105–120. https://doi.org/10.1016/j.actamat.2016.03.051.

[56] J.F. Ziegler, Nuclear instruments and methods in physics research section B: Beam interactions with materials and atoms, SRIM-2003. 219 (2004) 1027–1036.

[57] R.E. Stoller, M.B. Toloczko, G.S. Was, A.G. Certain, S. Dwaraknath, F.A. Garner, On the use of SRIM for computing radiation damage exposure, Nuclear Instruments and Methods in Physics Research Section B: Beam Interactions with Materials and Atoms. 310 (2013) 75–80. https://doi.org/10.1016/j.nimb.2013.05.008.

[58] J.-P. Crocombette, L. Van Brutzel, D. Simeone, L. Luneville, Molecular dynamics simulations of high energy cascade in ordered alloys: Defect production and subcascade division, Journal of Nuclear Materials. 474 (2016) 134–142. https://doi.org/10.1016/j.jnucmat.2016.03.020.

[59] David B. Williams, C. Barry Carter, Transmission Electron Microscopy: A Textbook for Materials Science, Springer US, n.d.

[60] D. Chen, K. Murakami, H. Abe, Z. Li, N. Sekimura, Investigation of interactions between defect clusters in stainless steels by in situ irradiation at elevated temperatures, Acta Materialia. 163 (2019) 78–90. https://doi.org/10.1016/j.actamat.2018.10.011.

[61] M.H. Loretto, R.E. Smallman, Defect analysis in electron microscopy, Chapman and Hall, New York, 1975.

[62] P.B. Hirsch, Electron microscopy of thin crystals, Plenum Press, 1967.

[63] M.L. Jenkins, Characterisation of radiation-damage microstructures by TEM, Journal of Nuclear Materials. 216 (1994) 124–156. https://doi.org/10.1016/0022-3115(94)90010-8.

[64] A. Howie, M.J. Whelan, Diffraction contrast of electron microscope images of crystal lattice defects. III. Results and experimental confirmation of the dynamical theory of dislocation image contrast, Proceedings of the Royal Society of London. Series A. Mathematical and Physical Sciences. 267 (1962) 206–230.

[65] A. Prokhodtseva, B. Décamps, A. Ramar, R. Schäublin, Impact of He and Cr on defect accumulation in ion-irradiated ultrahigh-purity Fe(Cr) alloys, Acta Materialia. 61 (2013) 6958–6971. https://doi.org/10.1016/j.actamat.2013.08.007.

[66] W. Wu, R. Schäublin, The elasticity of the ½ a0 and a0 dislocation loop in α-Fe thin foil, Journal of Nuclear Materials. 510 (2018) 61–69. https://doi.org/10.1016/j.jnucmat.2018.07.057.

[67] E. Toijer, L. Messina, C. Domain, J. Vidal, C.S. Becquart, P. Olsson, Solute-point defect interactions, coupled diffusion, and radiation-induced segregation in fcc nickel, Physical Review Materials. 5 (2021) 013602.

[68] L. Huang, M. Nastar, T. Schuler, L. Messina, Multiscale modeling of the effects of temperature, radiation flux, and sink strength on point-defect and solute redistribution in dilute Fe-based alloys, Physical Review Materials. 5 (2021) 033605.

[69] T. Schuler, L. Messina, M. Nastar, KineCluE: A kinetic cluster expansion code to compute transport coefficients beyond the dilute limit, Computational Materials Science. 172 (2020) 109191. https://doi.org/10.1016/j.commatsci.2019.109191.

[70] F.A. Nichols, On the estimation of sink-absorption terms in reaction-rate-theory analysis of radiation damage, Journal of Nuclear Materials. 75 (1978) 32–41. https://doi.org/10.1016/0022-3115(78)90026-0.

[71] L. Huang, K. Ma, L.T. Belkacemi, M. Loyer-Prost, E. Meslin, E. Toijer, L. Messina, C. Domain, J. Vidal, M. Nastar, Impact of the local microstructure fluctuations on radiation-induced segregation in dilute Fe-Ni and Ni-Ti model alloys: A combined modeling and experimental analysis, Acta Materialia. 225 (2022) 117531. https://doi.org/10.1016/j.actamat.2021.117531.

[72] J.M. Titchmarsh, S. Dumbill, On the measurement of radiation-induced segregation (RIS) at point defect sinks, Journal of Nuclear Materials. 227 (1996) 203–219. https://doi.org/10.1016/0022-3115(95)00159-X.

[73] J.T. Busby, G.S. Was, E.A. Kenik, Isolating the effect of radiation-induced segregation in irradiation-assisted stress corrosion cracking of austenitic stainless steels, Journal of Nuclear Materials. 302 (2002) 20–40. https://doi.org/10.1016/S0022-3115(02)00719-5.

[74] D. Ma, M. Friák, J. von Pezold, J. Neugebauer, D. Raabe, Ab initio study of compositional trends in solid solution strengthening in metals with low Peierls

stresses, Acta Materialia. 98 (2015) 367–376. https://doi.org/10.1016/j.actamat.2015.07.054.

[75] K. Kumar, R. Sankarasubramanian, U.V. Waghmare, Influence of dilute solute substitutions in Ni on its generalized stacking fault energies and ductility, Computational Materials Science. 150 (2018) 424–431. https://doi.org/10.1016/j.commatsci.2018.04.043.

[76] C. Varvenne, A. Luque, W.A. Curtin, Theory of strengthening in fcc high entropy alloys, Acta Materialia. 118 (2016) 164–176.

[77] L. Deléhouzée, A. Deruyttere, The stacking fault density in solid solutions based on copper, silver, nickel, aluminium and lead, Acta Metallurgica. 15 (1967) 727–734. https://doi.org/10.1016/0001-6160(67)90353-7.

[78] T. Jourdan, Influence of dislocation and dislocation loop biases on microstructures simulated by rate equation cluster dynamics, Journal of Nuclear Materials. 467 (2015) 286–301. https://doi.org/10.1016/j.jnucmat.2015.09.046.

[79] H. Rauh, D. Simon, On the diffusion process of point defects in the stress field of edge dislocations, Physica Status Solidi (a). 46 (1978) 499–510.

Appendix A. Calculation of radiation damage

Radiation damage (in dpa) and injected atom (in appm) are calculated by SRIM2013 [56] and IRADINA [58] codes and shown in Fig. A. 1.

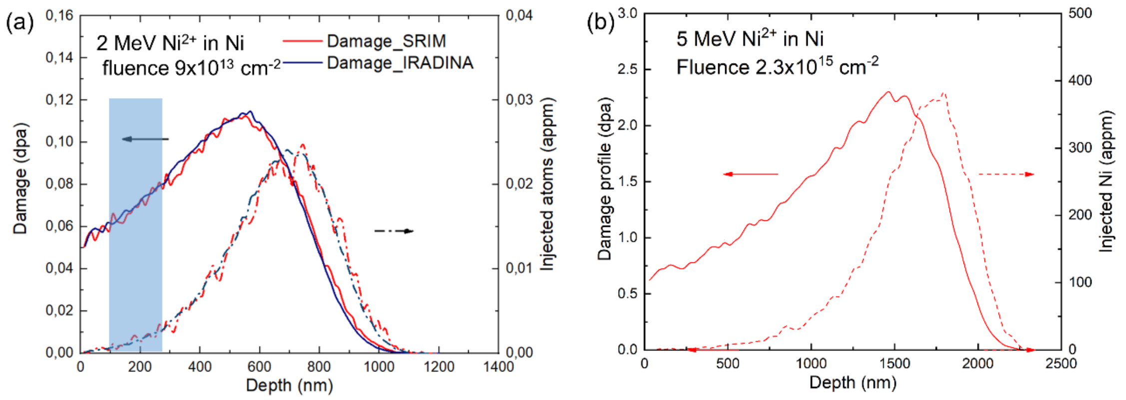

Fig. A. 1 Damage profile of (a) 2 MeV Ni^{2+} ions injected into Ni by SRIM 2013 code and IRADINA code for a fluence of 9×10^{13} ions.cm^{-2}; and (b) 5 MeV Ni^{2+} ions injected into Ni for a fluence of 2.3×10^{15} ions.cm^{-2} The displacement threshold energy of Ni is taken as 40 eV [3,57]

Appendix B. Loop density for loop type analysis

Loop densities in function of diffraction vector **g** in Ni-0.4Cr, Ni-0.4Ti, Ni-0.8Ti and Ni-1.2Ti irradiated at 510°C to 0.06 dpa are listed in Table B. 1 for the loop type analysis by statistic method. Loops are counted manually from TEM micrographs.

Table B. 1 Loop density (in 10^{20} loops/m^3) in function of diffraction vectors in Ni-0.4Cr, Ni-0.4Ti, Ni-0.8Ti and Ni-1.2Ti irradiated at 510°C to 0.06 dpa.

Ni-0.4Cr	Zone axes	[121]	[110]				[011]
	g investigated	$1\bar{1}1$	$\bar{1}1\bar{1}$	$\bar{1}11$	002	$\bar{2}20$	$\bar{1}\bar{1}1$
	Loop density	2.8	2.7	2.7	3.0	2.3	2.8

Ni-0.4Ti	Zone axes	[101]			$[1\bar{1}1]$			[001]
	g investigated	$11\bar{1}$	020	$1\bar{1}\bar{1}$	$20\bar{2}$	$\bar{2}0\bar{2}$	022	002
	Loop density	18.6	20.5	17.9	14.7	15.2	1.49	19.3

Ni-0.8Ti	Zone axes	[001]				$[1\bar{1}2]$
	g investigated	$2\bar{2}0$	$0\bar{2}0$	200	$\bar{2}\bar{2}0$	$\bar{1}11$
	Loop density	19.2	23.4	23.4	18.9	21.0

Ni-1.2Ti	Zone axes	[101]				[112]	[211]
	g investigated	$\bar{2}02$	$\bar{1}\bar{1}1$	020	$\bar{1}11$	$\bar{2}20$	$0\bar{2}2$
	Loop density	26.4	28.3	31.5	26.3	27.7	25.3

Appendix C. Microstructure in function of specimen thickness in Ni-Ti alloys

Fig. C. 1 shows the irradiated microstructure in Ni-0.4Ti, Ni-0.8Ti and Ni-1.2Ti thin foil irradiated at 510°C up to 0.06 dpa in function of specimen thickness. All TEM micrographs are taken using a diffraction vector **g**=<220>. Loop density and size are measured manually using Image J software.

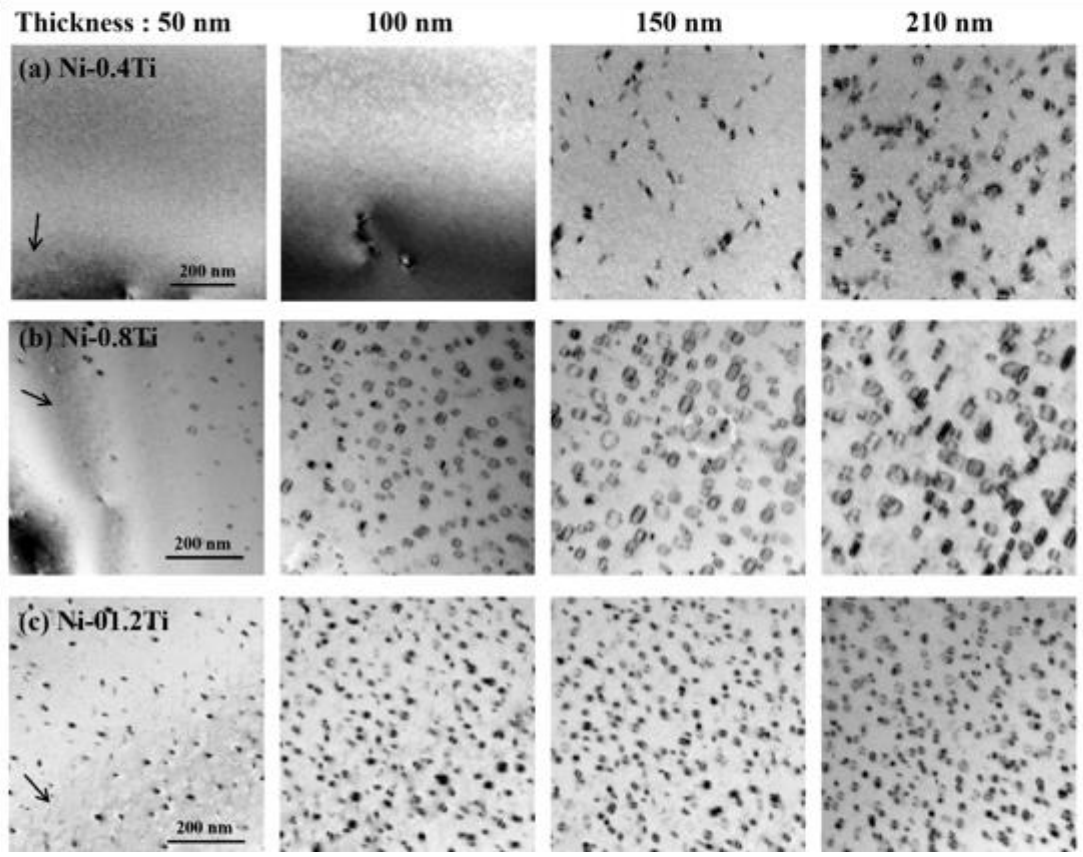

Fig. C. 1 TEM micrographs showing the microstructure in the same zones in function of specimen thickness in Ni-0.4/0.8/1.2Ti irradiated at 510°C to 0.06 dpa with **g**=<220> indicated by the black arrow.

Appendix D. Frank loop nature in Ni-0.4Cr and Ni-0.4Ti at 510°C

Fig. D. 1(a) and Fig. D. 1(b) present respectively the microstructure in Ni-0.4Cr and Ni-0.4Ti thin foils irradiated at 450°C to 0.7 dpa. Frank loops are detected in both materials. In Ni-0.4Cr, all Frank loops are segmented as shown by two typical loops in Fig. D. 1(c-d) and they are identified as vacancy-type. In Ni-0.4Ti, Frank loops are elliptic as shown in Fig. D. 1(e-f) and they are interstitial-type.

The thickness-dependency of loop density in Ni and Ni-0.4Ti is measured and plotted in Fig. D. 2.

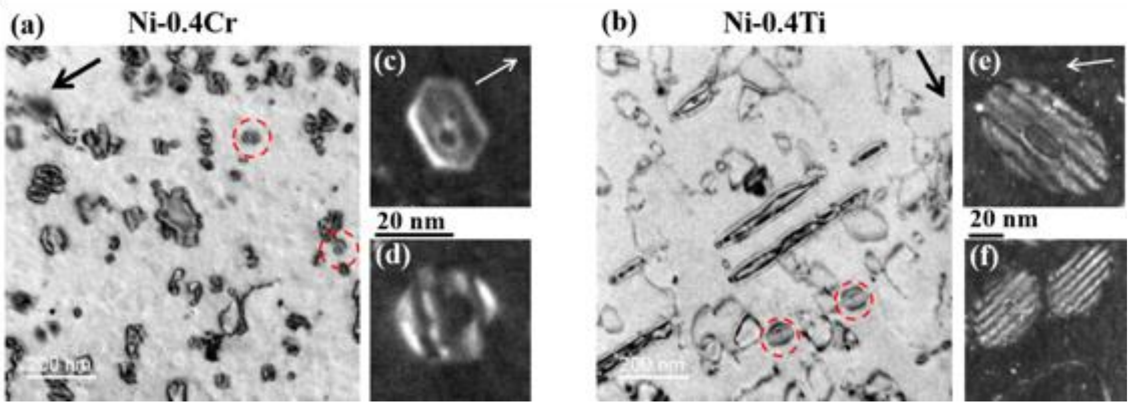

Fig. D. 1 Frank loops in thin foil of (a) Ni-0.4Cr and (b) Ni-0.4Ti irradiated to 0.7 dpa at 450°C by 5 MeV Ni^{2+} ions. BF images taken along zone axis <101> with (a) g={111} and (b) g={202} indicated by black arrows and several Frank loops encircled; WBDF images showing the morphology of Frank loops in (c-d) Ni-0.4Cr and (e-f) Ni-0.4Ti with g=<200> (white arrows).

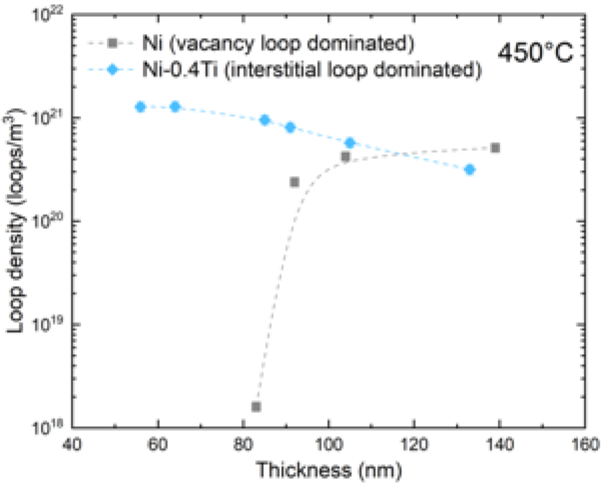

Fig. D. 2 Thickness dependency of loop density in function of thickness in Ni and Ni-0.4Ti irradiated at 450°C to 0.7 dpa by 5 MeV Ni^{2+} ions.

Appendix E. Calculation of interstitial loss

In our previous investigation [35], the steady-state variation of the vacancy loop radius, R, is written as:

$$\frac{dR}{dt} = \frac{\Omega}{b}\frac{Z_{l,i}}{k_i^2}G(1-\eta) + \frac{\Omega}{b}\left(Z_{l,v} - Z_{l,i}\frac{k_v^2}{k_i^2}\right)D_v C_v \qquad [35]$$

where Ω is the volume of a Ni atom, b is the Burgers vector of the loop, C_v is the atomic fraction of vacancies, D_v is diffusion coefficients of vacancies, $Z_{l,v}$ and $Z_{l,i}$ are adsorption efficiency of the loop for vacancies and interstitials, k_v^2 and k_i^2 are the total sink strengths for vacancies and interstitials respectively, G is the production rate of PDs in dpa/s, and $(1-\eta)$ is the loss fraction of interstitials due to the 1D motion of I-clusters.

To deduce the interstitial loss rate, the parameters in Eq.(1) is calculated as the following. D_v is deduced from [67], C_v is deduced using the rate theory model in [68], Z_i and Z_v the absorption factor for interstitials and vacancies by loops deduced from [78], $k_{\text{surf}}^2 = 12/t^2$ where t is the thickness [70], G=2.7x10^{-4} dpa/s. The used parameters are shown in the following table with the total sink strength k^2_{V} and k^2_{I} is the sum of k^2_{surface} and k^2_{loop}. In Ni the sink strength of dislocation network $k^2_{\text{line,V}}$ = 9x10^{12} m^{-2} (density = 8x10^{12} m^{-2}) from the analytical expression in [79]. Each k^2 is calculated using formulae in [70,78]. The critical loss in Ni in this study is slightly different from a previous work [35] as model and used parameters are different. The diffusion coefficients here are calculated using more recent DFT data, the bias is calculated based on specific absorption factors and the sink strength of loops and of dislocation lines are different here.

Table E. 1 Parameters used for interstitial rate calculations

	Thickness (x10^{-7} m)	k^2_{surface} (m^{-2})	loop density (loops/m3)	loop diam. (nm)	Z_V	Z_I	k^2_V (m^{-2})	k^2_I (m^{-2})	B_I	C_V
Ni	2,6	1,78E+14	8,1E+20	21,1	1,49	1,67	2,7E+14	2,8E+14	3,8E-2	3,15E-6
Ni-0.4Cr	2,2	2,48E+14	2,2E+20	34,6	1,35	1,50	2,8E+14	2,8E+14	1,3E-2	2,99E-6
Ni-0.4Ti	2,2	2,48E+14	1,9E+21	13,6	1,63	1,84	3,8E+14	4,0E+14	4,3E-2	2,21E-6
Ni-0.8Ti	1,2	8,33E+14	3,1E+21	12,2	1,68	1,90	1,0E+15	1,1E+15	2,5E-2	8,13E-7
Ni-1.2Ti	1,2	8,33E+14	5,8E+21	11,2	1,75	1,99	1,2E+15	1,2E+15	3,9E-2	7,05E-7

Appendix F. Calculation of point defects contained in loops

The total PD number (either vacancy number or interstitial number) contained in loops is calculated as $\pi d D^2/(4SN)$ as a fraction concentration (in PDs/atom) with d the loop density, D the average size (diameter), S=5.36x10^{-2} nm^2 the atom cross-section area on <111> planes, N=94 atoms/nm^3 the number of Ni atoms in unit volume.